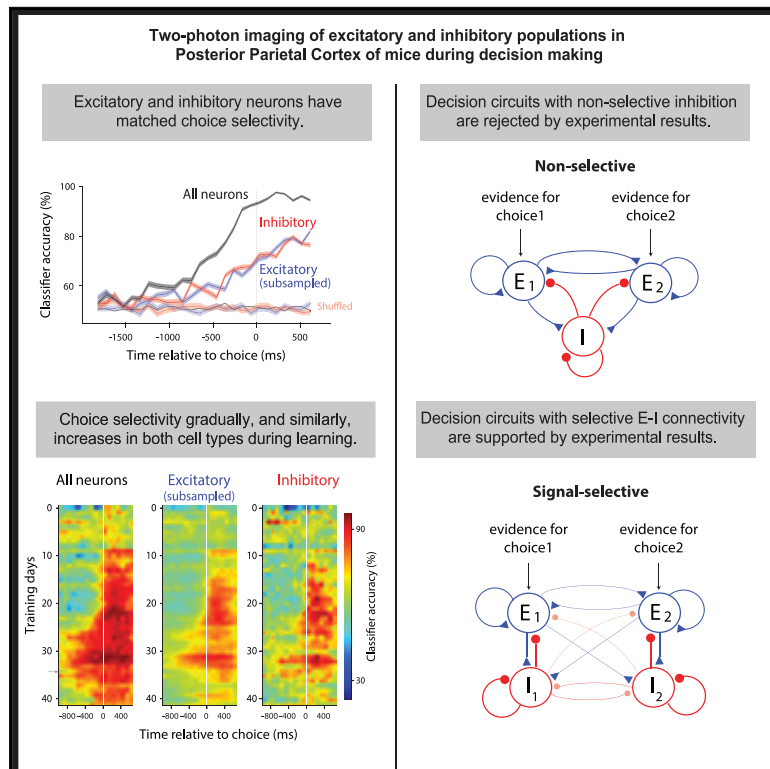# Excitatory and Inhibitory Subnetworks Are Equally Selective during Decision-Making and Emerge Simultaneously during Learning

## Graphical Abstract



Two-photon imaging of excitatory and inhibitory populations in Posterior Parietal Cortex of mice during decision making

Excitatory and inhibitory neurons have matched choice selectivity.

Decision circuits with non-selective inhibition are rejected by experimental results.

Choice selectivity gradually, and similarly, increases in both cell types during learning.

Decision circuits with selective E-I connectivity are supported by experimental results.

## Authors

Farzaneh Najafi,
Gamaleldin F. Elsayed, Robin Cao,
Eftychios Pnevmatikakis,
Peter E. Latham, John P. Cunningham,
Anne K. Churchland

## Correspondence

achurchl@cshl.edu

## In Brief

Najafi et al. studied selectivity of mouse excitatory and inhibitory neurons during decision-making. Selectivity is equally strong in the two cell types and emerges gradually during learning. These data, along with theoretical models, argue that selective subnetworks support decision-making.

## Highlights

- Excitatory and inhibitory neurons are equally selective during decision-making

- Selectivity of the two cell types increases in parallel during learning

- Models and experiments reject decision circuits with non-selective inhibition

- Selective subnetworks of neurons emerge during learning to support decision-making

**CellPress**

**Cell**Press

# Excitatory and Inhibitory Subnetworks Are Equally Selective during Decision-Making and Emerge Simultaneously during Learning

Farzaneh Najafi,[1,6] Gamaleldin F. Elsayed,[2,7] Robin Cao,[3] Eftychios Pnevmatikakis,[4] Peter E. Latham,[3] John P. Cunningham,[5] and Anne K. Churchland[1,8,*]

[1]Cold Spring Harbor Laboratory, Cold Spring Harbor, NY 11724, USA
[2]Neuroscience, Columbia University, New York, NY 10027, USA
[3]Gatsby Computational Neuroscience Unit, University College London, London, UK
[4]Flatiron Institute, New York, NY, USA
[5]Statistics, Columbia University, New York, NY 10010, USA
[6]Present address: Allen Institute for Brain Sciences, Seattle, WA 98109, USA
[7]Present address: Google Research, Brain Team, Mountain View, CA 94043, USA
[8]Lead Contact
*Correspondence: achurchl@cshl.edu
https://doi.org/10.1016/j.neuron.2019.09.045

## SUMMARY

Inhibitory neurons, which play a critical role in decision-making models, are often simplified as a single pool of non-selective neurons lacking connection specificity. This assumption is supported by observations in the primary visual cortex: inhibitory neurons are broadly tuned *in vivo* and show non-specific connectivity in slice. The selectivity of excitatory and inhibitory neurons within decision circuits and, hence, the validity of decision-making models are unknown. We simultaneously measured excitatory and inhibitory neurons in the posterior parietal cortex of mice judging multisensory stimuli. Surprisingly, excitatory and inhibitory neurons were equally selective for the animal's choice, both at the single-cell and population level. Further, both cell types exhibited similar changes in selectivity and temporal dynamics during learning, paralleling behavioral improvements. These observations, combined with modeling, argue against circuit architectures assuming non-selective inhibitory neurons. Instead, they argue for selective subnetworks of inhibitory and excitatory neurons that are shaped by experience to support expert decision-making.

## INTRODUCTION

In many decisions, noisy evidence is accumulated over time to support a categorical choice. At the neural level, a number of models can implement evidence accumulation (Wang, 2002; Machens et al., 2005; Bogacz et al., 2006; Lo and Wang, 2006; Wong and Wang, 2006; Beck et al., 2008; Lim and Goldman, 2013; Rustichini and Padoa-Schioppa, 2015; Mi et al., 2017). Although these circuit models successfully reproduce key char-

acteristics of behavioral and neural data during perceptual decision-making, their empirical evaluation has been elusive, mainly because of the challenge of identifying inhibitory neurons reliably and in large numbers in behaving animals. Inhibition, which constitutes an essential component of these models, is usually provided by a single pool of inhibitory neurons receiving broad input from all excitatory neurons (non-selective inhibition; Deneve et al., 1999; Wang, 2002; Mi et al., 2017).

The assumption of non-selective inhibition in theoretical models was perhaps motivated by empirical studies examining connectivity and tuning of inhibitory neurons. Many studies of the primary visual cortex report that inhibitory neurons have, on average, broader tuning curves than excitatory neurons for visual stimulus features such as orientation (Sohya et al., 2007; Niell and Stryker, 2008; Liu et al., 2009; Kerlin et al., 2010; Bock et al., 2011; Hofer et al., 2011; Atallah et al., 2012; Chen et al., 2013; Znamenskiy et al., 2018), spatial frequency (Niell and Stryker, 2008; Kerlin et al., 2010; Znamenskiy et al., 2018), and temporal frequency (Znamenskiy et al., 2018). Broad tuning in inhibitory neurons has been mostly attributed to their dense (Hofer et al., 2011; Packer and Yuste, 2011), functionally unbiased inputs from surrounding excitatory neurons (Kerlin et al., 2010; Bock et al., 2011; Hofer et al., 2011). Excitatory neurons, in contrast, show relatively sharp selectivity to stimulus features (Sohya et al., 2007; Niell and Stryker, 2008; Ch'ng and Reid, 2010; Kerlin et al., 2010; Hofer et al., 2011; Isaacson and Scanziani, 2011; Lee et al., 2016), reflecting their specific, non-random connectivity (Yoshimura et al., 2005; Ch'ng and Reid, 2010; Hofer et al., 2011; Ko et al., 2011; Cossell et al., 2015; Ringach et al., 2016).

Based on relatively weak tuning of inhibition, one might assume that inhibition in decision circuits is non-specific. However, the overall picture from experimental observations is more nuanced than the original studies suggest. First, some primary visual cortex (V1) studies report tuning of inhibitory neurons that is on par with excitatory neurons (Ma et al., 2010; Runyan et al., 2010), likely supported by targeted connectivity with excitatory neurons (Yoshimura and Callaway, 2005). Strong tuning of
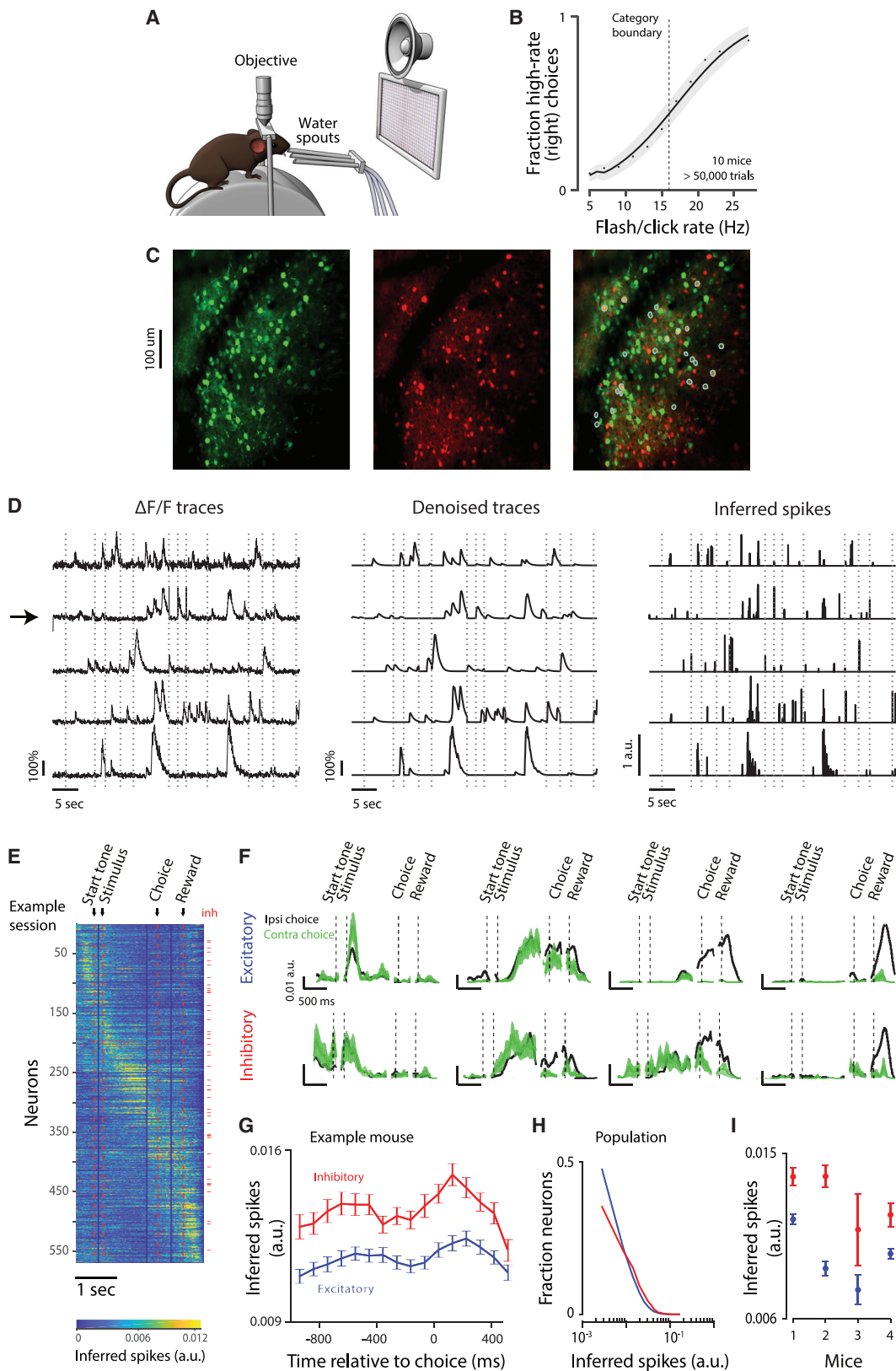
*(legend on next page)*

inhibitory neurons has also been reported in the primary auditory cortex (Moore and Wehr, 2013). Further, in the frontal and parietal areas, interneurons can distinguish go versus no-go responses (Allen et al., 2017) and trial outcome (Pinto and Dan, 2015). Similarly, hippocampal interneurons have strong selectivity for the stimulus (Lovett-Barron et al., 2014) and the animal's location (Maurer et al., 2006; Ego-Stengel and Wilson, 2007).

This selectivity of inhibitory neurons in a wealth of areas and conditions argues that the assumption of non-selective interneurons in decision-making models must be revisited. Here we aimed to evaluate this directly. We compared the selectivity of inhibitory and excitatory neurons in the posterior parietal cortex (PPC) in mice during perceptual decisions. Surprisingly, we found that excitatory and inhibitory neurons are equally choice selective. Our modeling argued that these observations imply selective subnetworks, a network architecture supporting enhanced decoding in the presence of noise. Finally, during learning, the selectivity of excitatory and inhibitory neurons increased in parallel. These results constrain decision-making models and argue that, in decision areas, subnetworks of selective inhibitory neurons emerge during learning and are engaged during expert decisions.

## RESULTS

To test how excitatory and inhibitory neurons coordinate during decision-making, we measured neural activity in transgenic mice trained to report decisions about the repetition rate of a sequence of multisensory events by licking a left or right waterspout (Figure 1A; Figure S1A). Trials consisted of simultaneous clicks and flashes, generated randomly (via a Poisson process) at rates of 5–27 Hz over 1,000 ms (Brunton et al., 2013; Odoemene et al., 2018). Mice reported whether event rates were high or low compared with a category boundary (16 Hz) learned from experience. Decisions depended strongly on the stimulus rate; performance was at chance when the stimulus rate was

at the category boundary and better at rates further from the category boundary (Figure 1B). Choice depended on current stimulus strength, previous choice outcome (Hwang et al., 2017), and time elapsed since the previous trial (Figure S1B).

We imaged excitatory and inhibitory neural activity by injecting a viral vector containing the calcium indicator (GCaMP6f) to layer 2/3 of the mouse PPC (Harvey et al., 2012; Funamizu et al., 2016; Goard et al., 2016; Morcos and Harvey, 2016; Hwang et al., 2017; Song et al., 2017). Mice expressed the red fluorescent protein tdTomato transgenically in all GABAergic inhibitory neurons (STAR Methods). We used a two-channel, two-photon microscope to record the activity of all neurons, a subset of which were identified as inhibitory (Figure 1C). This allowed us to measure the activity of excitatory and inhibitory populations in the same animal.

To detect neurons and extract calcium signals, we leveraged an algorithm that simultaneously identifies neurons, de-noises the fluorescence signal, and de-mixes signals from spatially overlapping components (Pnevmatikakis et al., 2016; Giovannucci et al., 2019; Figure 1D, center). The algorithm also estimates spiking activity for each neuron, yielding, for each frame, a number that is related to the spiking activity during that frame (Figure 1D, right). We refer to this number as "inferred spiking activity," acknowledging that estimating spikes from calcium signals is challenging (Chen et al., 2013). Analyses were performed on inferred spiking activity. To identify inhibitory neurons, we developed a method to correct for bleed-through from the green to the red channel (STAR Methods). We identified a subset of GCaMP6f-expressing neurons as inhibitory based on signal intensity (red channel) and spatial correlation between red and green channels (Figure 1C, right, cyan circles). Inhibitory neurons constituted 11% of the population, within the range of previous reports (Beaulieu, 1993; Gabbott et al., 1997; Rudy et al., 2011; Sahara et al., 2012) but on the lower side because of our desire to be conservative in assigning neurons to the inhibitory pool (STAR Methods).

**Figure 1. Simultaneous Imaging of Inhibitory and Excitatory Populations during Decision-Making**

(A) Behavioral apparatus. Multisensory stimuli are presented via a visual display and a speaker. To initiate trials, mice lick the middle waterspout. To report decisions about stimulus rate, mice lick left/right spouts. Objective: a 2-photon microscope used to image neural activity through an implanted window.

(B) Psychometric function showing the fraction of trials in which the mouse chose "high" as a function of stimulus rate. Dots, mean (10 mice); line, logit regression model (glmfit.m), mean across mice; shaded area, SD of the fit across mice; dashed vertical line, category boundary (16 Hz).

(C) Average image (10,000 frames). Left: green channel, GCaMP6f. Center: red channel, tdTomato. Right: merge of left and center. Cyan circles, GCaMP6f-expressing neurons identified as inhibitory.

(D) Example neurons identified by the constrained non-negative matrix factorization algorithm (STAR Methods). Arrow, inhibitory neuron. Left: raw ΔF/F traces. Center: de-noised traces. Right: inferred spiking activity. Imaging was not performed during inter-trial intervals; traces from 13 consecutive trials are concatenated. Dashed lines, trial onset.

(E) Example session; 568 neurons. Rows, trial-averaged inferred spiking activity of a neuron (frame resolution, 32.4 ms). Neurons are sorted based on timing of peak activity. To ensure peaks were not driven by noisy fluctuations, we first computed trial-averaged activity using 50% of trials for each neuron. We then identified the peak activity time for the trial-averaged response. Finally, these peak times determined the plotting order for the trial-averaged activity for the remaining 50% of trials. This cross-validated approach ensured that the tiling appearance of peak activities was not due to the combination of sorting and false-color plotting. Red ticks on the right, inhibitory neurons (n = 45); red vertical lines, trial events. Duration between events varied across trials. To make trial-averaged traces, traces were separately aligned to each trial event and then averaged across trials. Next, averaged traces (each aligned to a different trial event) were concatenated. Vertical blue lines, border between the concatenated traces.

(F) Trial-averaged inferred spiking activity of 4 excitatory (top) and 4 inhibitory (bottom) neurons for ipsilateral (black) and contralateral (green) choices (mean ± SEM, ~250 trials per session).

(G) Inferred spiking activity for excitatory (blue) and inhibitory (red) neurons. Example mouse; mean ± SEM across days (n = 46). Each point corresponds to an average over trials and neurons. Inferred spiking activity was downsampled by averaging over three adjacent frames (STAR Methods).

(H) Distribution of inferred spiking activity 0–97 ms before choice (averaged over three frames) for all mice/sessions (41,723 excitatory and 5,142 inhibitory).

(I) Inferred spiking activity 0–97 ms before the choice (averaged over three frames) for individual mice (mean ± SEM across days).
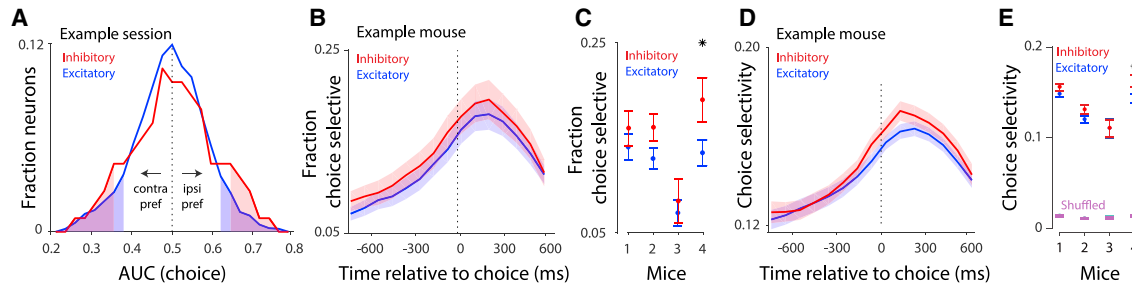
**Figure 2. Single-Cell and Pairwise Analyses Argue for Non-random Connections between Excitatory and Inhibitory Neurons**
(A) Distribution of AUC (area under the curve) values of an ROC analysis for distinguishing choice from the activity of single neurons in an example session. Data correspond to the 97-ms window preceding choice (285 excitatory and 29 inhibitory neurons). Values larger than 0.5 indicate a preference for ipsilateral choice; values smaller than 0.5 indicate a preference for contralateral choice. Shaded areas, significant AUC values (compared with a shuffle distribution). Distributions were smoothed (moving average, span = 5). 5 inhibitory and 24 excitatory neurons (17% and 8%, respectively) were significantly choice selective.
(B) ROC analysis on 97-ms non-overlapping time windows. Vertical axis, fraction of excitatory or inhibitory neurons with significant choice selectivity; example mouse; mean ± SEM across days (n = 45 days).
(C) Fraction of excitatory and inhibitory neurons that are significantly choice selective (0–97 ms before the choice) summarized for each mouse; mean ± SEM across days (n = 45, 48, 7, and 35 sessions per mouse). t test, *p < 0.05; see also Figure S3D. Fraction-selective neurons at 0–97 ms before choice (median across mice): excitatory, 13%; inhibitory, 16% (~6 inhibitory and 43 excitatory neurons with significant choice selectivity per session).
(D) ROC analysis for 97-ms non-overlapping time windows; time course of normalized choice selectivity (defined as twice the absolute deviation of the AUC from chance, given explicitly by 2*|AUC-0.5|) for excitatory and inhibitory neurons in an example mouse; mean ± SEM across days, n = 45 sessions.
(E) Average of normalized choice selectivity for excitatory and inhibitory neurons (0–97 ms before choice) summarized for each mouse; mean ± SEM across days. "Shuffled" denotes that the AUC was computed using shuffled trial labels.
Blue and red indicate excitatory and inhibitory neurons, respectively.

Confirming previous reports (Funamizu et al., 2016; Morcos and Harvey, 2016; Runyan et al., 2017), we observed that the activity of individual neurons peaked at time points spanning the trial (Figures 1E and 1F). Diverse temporal dynamics were evident in both cell types (Figures 1E and 1F) and did not appreciably differ between the two (Figure S2). The magnitude of inferred spiking activity was significantly different for inhibitory versus excitatory neurons throughout the trial (Figure 1G; t test, p < 0.001). Just before the choice (97 ms, average of 3 frames), this difference was clear (Figure 1H) and significant for all mice (Figure 1I; t test; p < 0.001). Differences in GCaMP expression levels and calcium buffering between excitatory and inhibitory neurons, as well as how spiking activity is inferred (STAR Methods), make direct estimates of the underlying firing rates challenging (Kwan and Dan, 2012). Nevertheless, the significant difference in the inferred spiking activity between excitatory and inhibitory neurons provides additional evidence that we successfully identified two separate neural populations.

### Individual Excitatory and Inhibitory Neurons Are Similarly Choice Selective

To assess the selectivity of individual excitatory and inhibitory neurons for decision outcome, we performed a receiver operating characteristic (ROC) analysis (Green and Swets, 1966) on single-neuron responses. A neuron was identified as "choice selective" when the area under the ROC curve (AUC) differed significantly (p < 0.05) from a shuffled distribution (Figure S3A; STAR Methods), indicating that the neural activity differed significantly for ipsi- versus contralateral choices (Figure 2A).

The fraction of choice-selective neurons (Figure 2B) and the magnitude of choice selectivity (Figure 2D) gradually increased over the trial, peaking just after the animal reported its choice. Importantly, excitatory and inhibitory neurons were similar in

terms of the fraction of choice-selective neurons (Figures 2B and 2C; Figures S3B and S3C) as well as the magnitude and time course (Figures 2D and 2E) of choice selectivity. When we restricted the analysis to excitatory and inhibitory neurons with similar spiking activity, the cell types remained equally selective for the animal's choice (Figure S3D).

To assess whether neurons reflected the animal's choice or the sensory stimulus, we compared choice selectivity on correct versus error trials. For most neurons, choice selectivity on correct trials was similar to that on error trials, resulting in a positive correlation of the two quantities across neurons (Figure S3E). Positive correlations indicate that most neurons reflect the impending choice more so than the sensory stimulus that informed it (STAR Methods). Variability across mice in the strength of this correlation may indicate that the balance of sensory versus choice signals within individual neurons varied across subjects (perhaps because of imaged subregions within the window; Figure S3E, right). Importantly, however, within each subject, this correlation was very similar for excitatory versus inhibitory neurons (Figure S3E), suggesting that the tendency for neurons to be modulated by the choice versus the stimulus was similar in excitatory and inhibitory neurons.

The existence of task-modulated inhibitory neurons has been reported elsewhere (Maurer et al., 2006; Ego-Stengel and Wilson, 2007; Lovett-Barron et al., 2014; Pinto and Dan, 2015; Allen et al., 2017; Kamigaki and Dan, 2017), but, importantly, here choice selectivity was similarly strong in excitatory and inhibitory neurons, both in fraction and magnitude. This was at odds with the commonly accepted assumption of non-specific inhibition in theoretical studies (Deneve et al., 1999; Wang, 2002; Mi et al., 2017) and surprising given the numerous empirical findings suggesting broad tuning and weakly specific connectivity in inhibitory neurons (Sohya et al., 2007; Niell and Stryker, 2008;

Liu et al., 2009; Kerlin et al., 2010; Bock et al., 2011; Hofer et al., 2011; Isaacson and Scanziani, 2011; Packer and Yuste, 2011; Atallah et al., 2012; Chen et al., 2013). This observation was a first hint that specific functional subnetworks, preferring either ipsi- or contralateral choices, exist within the inhibitory population, just like in the excitatory population (Yoshimura and Callaway, 2005; Znamenskiy et al., 2018).

## Choice Is Decoded with Equal Accuracy from Both Excitatory and Inhibitory Populations

Although individual inhibitory neurons could distinguish the animal's choice as well as excitatory ones, overall choice selectivity in single neurons was small (Figure 2E). To further evaluate the neurons' discriminability, we trained linear classifiers (support vector machine [SVM]; Hofmann et al., 2008) to predict the mouse's choice from the single-trial population activity (cross-validated, L2 penalty; STAR Methods).

We first tested all neurons imaged simultaneously in a single session (Figure 3A, left), training the classifier separately at each time point (97 ms bins). Classification accuracy gradually grew after stimulus onset and peaked at the time of the choice (Figure 3B, black). The ability of the entire population of PPC neurons to predict the choice confirms previous observations (Funamizu et al., 2016; Goard et al., 2016; Morcos and Harvey, 2016; Driscoll et al., 2017). Our overall classification accuracy was in the same range as these studies and, as in those studies, was high, although many individual neurons in the population were only weakly selective (Figure 2A).

We then examined classifier accuracy for excitatory and inhibitory populations, subsampling the excitatory population so that the total number of neurons was matched (Figure 3A, center). The overall classification accuracy was reduced because of the smaller population size, but performance was still well above chance (Figure 3B, blue trace). Finally, we included all inhibitory neurons (Figure 3A, right). The classification accuracy of inhibitory neurons was well above chance and very similar to that of excitatory neurons (Figure 3B, red and blue traces overlap; see Figure S4 for additional example sessions). A similar classification accuracy for excitatory and inhibitory populations was observed in all subjects (Figure 3C). Excitatory and inhibitory populations were equally choice selective even when the analysis was performed on raw calcium traces (Figure S5).

Our analysis may have obscured a difference between excitatory and inhibitory neurons because we evaluated their performance separately rather than considering how these neurons are leveraged collectively in a classifier with both cell types. To test this, we examined a classifier that was trained on all neurons (Figures 3A, left, and 3B, black), and compared classifier weights assigned to excitatory versus inhibitory neurons. The weight magnitudes of excitatory and inhibitory neurons were matched for the entire trial (Figure 3D), and the distribution of weights was very similar (Figures 3E and 3F). The comparable classifier weights for excitatory and inhibitory neurons argues that these cell types are similarly informative for choice.

We next tested whether excitatory and inhibitory populations can be decoded more accurately from a mixed population. This can occur, for example, when the excitatory-inhibitory cor-

relations are weak relative to excitatory-excitatory and inhibitory-inhibitory correlations (Panzeri et al., 1999; Averbeck et al., 2006; Moreno-Bote et al., 2014). To assess this, we trained the classifier on a population with half excitatory and half inhibitory neurons (Figure 3G, bottom) and compared its accuracy with a classifier trained on a population of the same size that consisted only of excitatory neurons (Figure 3G, top). The classification accuracy was similar for both decoders (Figures 3H and 3I), arguing that a mixed population offers no major advantage for decoding.

We next trained new classifiers to evaluate whether population activity reflected additional task features. First, the population activity was somewhat informative regarding previous trial choice (Figure S6A), in agreement with previous studies (Morcos and Harvey, 2016; Hwang et al., 2017; Akrami et al., 2018; but see also Zhong et al., 2019). Excitatory and inhibitory populations were similarly selective for previous choice (Figure S6A). The population activity was also somewhat informative regarding whether the stimulus was above or below the category boundary (Figure S6B). Again, excitatory and inhibitory populations were similarly selective (Figure S6B). Finally, the population activity was strongly selective for trial outcome (reward versus lack of reward; Figure S6C). Excitatory and inhibitory neurons showed a small but consistent difference in classifier accuracy after reward delivery (Figure S6C). This indicates that, when the reward is delivered, the network enters a new regime, perhaps because of distinct reward-related inputs to excitatory and inhibitory neurons (Pinto and Dan, 2015; Allen et al., 2017). This possibility is in keeping with previous studies suggesting that neural populations explore different dimensions over the course of a trial (Raposo et al., 2014; Elsayed et al., 2016).

Finally, we studied the temporal dynamics of the choice signal. If excitatory and inhibitory neurons form connected subnetworks with frequent cross-talk, then the two populations should not only predict the animal's choice with similar accuracy, as shown above, but the weights assigned by the classifier should exhibit similar temporal dynamics. To assess this, we quantified each population's stability: the extent to which a classifier trained on choice at one time could successfully classify choice at other times. If population activity patterns are similar over time (e.g., all neurons gradually increase their firing rates), then classifiers trained at one moment will accurately classify neural activity at different moments. Excitatory and inhibitory populations might differ in this regard, with one population more stable than the other.

As the gap between testing and training time increased, a gradual drop occurred in classifier accuracy (Figures 4A and 4B). This drop in accuracy occurred at a similar rate for excitatory and inhibitory populations (Figure 4B). To quantify this, we determined the time window over which classifier accuracy remained within 2 SDs of the accuracy at the training time (Figure 4C). This was indistinguishable for excitatory and inhibitory neurons (Figure 4D; Figure S7A). An alternate method for assessing stability, computing the angle between the weights of pairs of classifiers trained at different time windows, likewise suggested that excitatory and inhibitory populations are similarly stable (STAR Methods; Figure S7C).
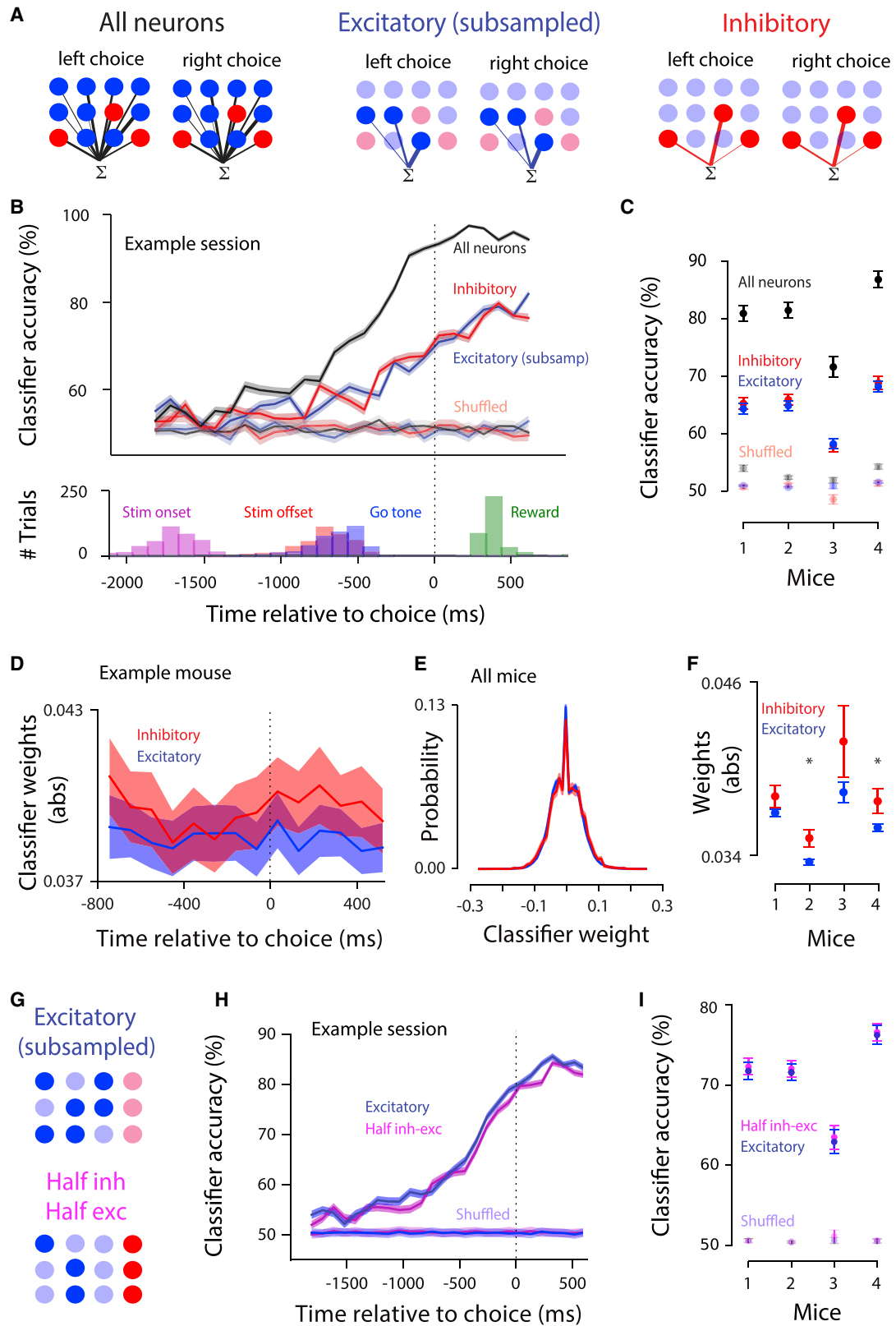
(legend on next page)
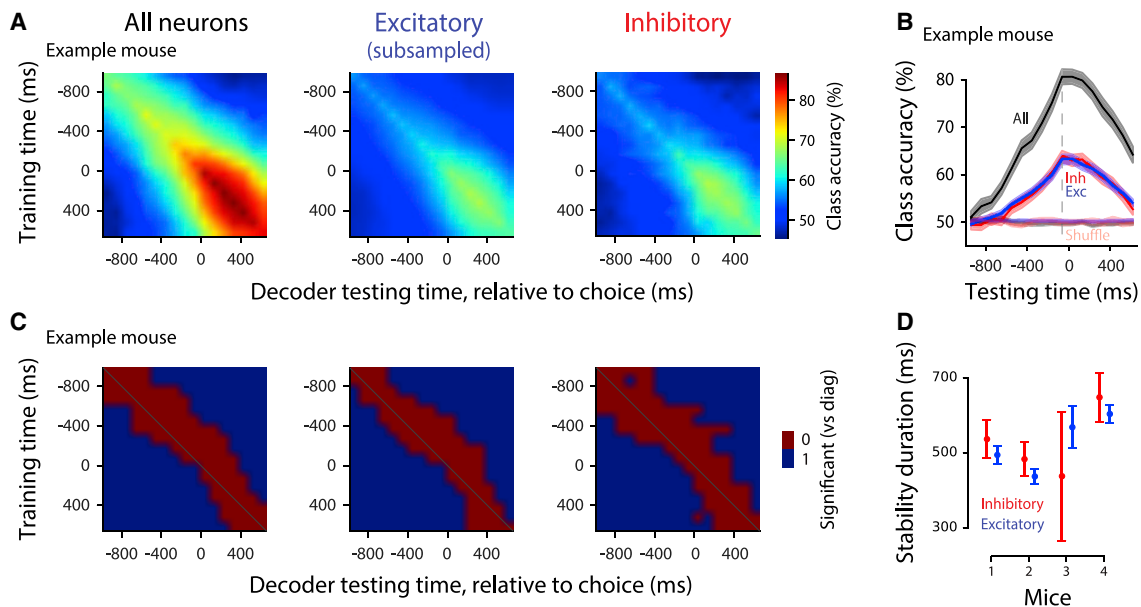
**Figure 4. Classifiers, Whether Trained on Excitatory or Inhibitory Neurons, Show Comparable Stability during Decision Formation**

Shown is cross-temporal generalization of choice decoders.

(A) Classification accuracy of decoders for each pair of training/testing time points, for all neurons (left), subsampled excitatory neurons (center), or inhibitory neurons (right). Diagonal, same training and testing time as in Figure 3. Example mouse, mean across 45 sessions.

(B) Example classification accuracy traces showing how classifiers trained at 0–97 ms before choice generalize across time. Same mouse as in (A), mean ± SEM across days.

(C) Decoders are stable in a short window outside of their training time. Red indicates that classification accuracy of a decoder tested at the time on the horizontal axis is 2 SDs or less of the decoder tested at the training time. Example mouse, mean across days.

(D) Summary of stability duration for decoders trained from 0–97 ms before choice using inhibitory neurons (red) or subsampled excitatory neurons (blue). Mean ± SEM across days per mouse.

## Modeling Rules Out Decision Circuits with Non-selective Inhibition

These results seem to rule out circuitry from traditional decision-making models in which inhibitory neurons are non-selective. This is because, in non-selective circuits, the average input to inhibitory neurons is the same whether the evidence favors choice 1 or choice 2 (Figure 5A, top). However, care must be taken when drawing this conclusion. Although the average input is the same, there are fluctuations in connection strength; those fluctuations will lead to some selectivity in inhibitory neurons. For instance, because of the inherent randomness in neural circuits, an inhibitory neuron could receive more connections from the excitatory neurons in population $E_1$ versus $E_2$. If so, then the firing rate of that inhibitory neuron would be slightly higher when evidence in favor of choice 1 is present. This could be exploited by a classifier to predict the choice. Hence, even a decision circuit with non-selective inhibition (Figure 5A, top) can lead to similar decoding accuracy in inhibitory and excitatory neurons, questioning whether our experimental findings (Figures 2 and 3) can be leveraged to constrain decision-making models.

**Figure 3. Linear Classifiers Can Predict the Animal's Choice with Equal Accuracy from the Activity of Excitatory or Inhibitory Populations**

(A) Schematic of decoding choice from all neurons (left), only excitatory neurons (center) subsampled to the same number as inhibitory neurons, and only inhibitory neurons (right). A linear SVM assigns weights of different magnitude (indicated by lines of different thickness) to each neuron in the population.

(B) Top: classification accuracy of decoders trained on all neurons (black), subsampled excitatory neurons (blue), and inhibitory neurons (red) (cross-validated; decoders trained on every 97-ms time bin; example session; mean ± SEM across 50 cross-validated samples). Data are aligned to the animal's choice (black dotted line). Unsaturated lines, performance on shuffled trials. Bottom: distribution of stimulus onset, offset, go tone, and reward occurrence for the example session above.

(C) Classification accuracy (0–97 ms before the choice, mean ± SEM across days) for real (saturated) and shuffled (unsaturated) data.

(D) Absolute value of weights for excitatory and inhibitory neurons in decoders trained on all neurons; mean ± SEM across days.

(E) Distribution of classifier weights (decoder training time, 0–97 ms before the choice) for excitatory and inhibitory neurons. Neurons from all mice were pooled (42,019 excitatory and 5,172 inhibitory neurons). Shading, SE.
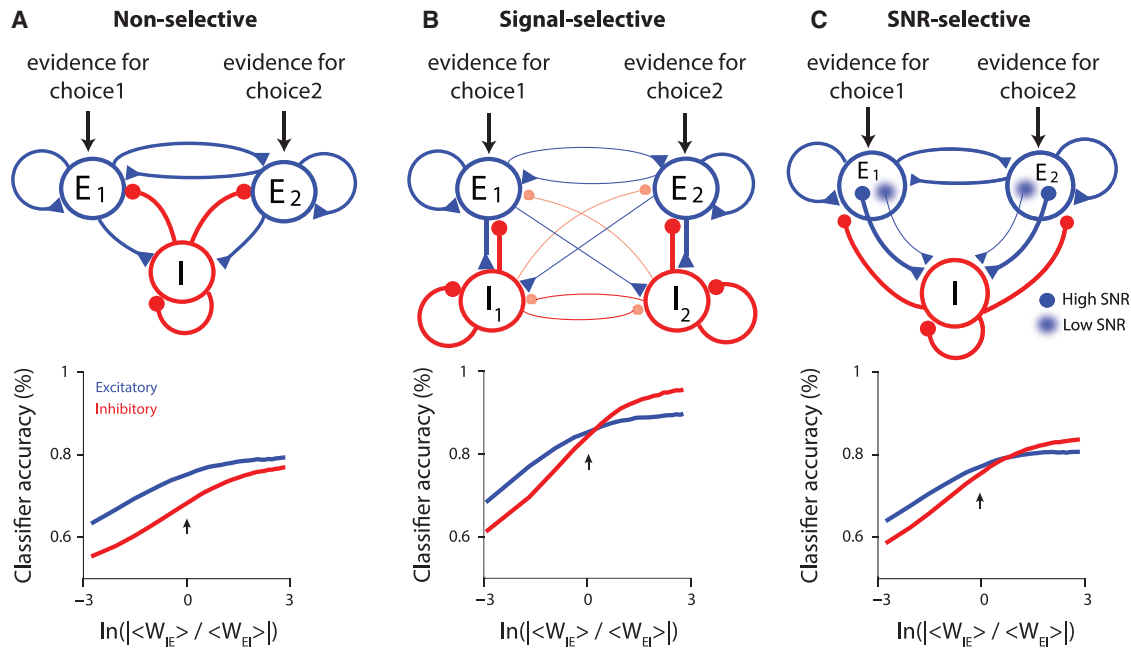
(F) Absolute value of weights in the classifier (0–97 ms before choice) for excitatory versus inhibitory neurons. Mean ± SEM across days. *p < 0.05, t test.

(G) Schematic of decoding choice from a population of subsampled excitatory neurons (top) versus a population with half inhibitory and half excitatory neurons (bottom).

(H) Classifier accuracy of populations including only excitatory (blue) or half inhibitory and half excitatory neurons (magenta); example session; classifier trained at each moment in the trial. Traces show mean ± SEM (50 cross-validated samples).

(I) Summary of each mouse (mean ± SEM across days) for the decoders (0–97 ms before the choice).

**A** Non-selective

evidence for choice1          evidence for choice2

**B** Signal-selective

evidence for choice1          evidence for choice2

**C** SNR-selective

evidence for choice1          evidence for choice2

High SNR
Low SNR

Excitatory
Inhibitory

**Figure 5. Modeling Decision Circuits with Different Architectures**

(A) Top: non-selective decision-making model. $E_1$ and $E_2$, pools of excitatory neurons, each favoring a different choice, that excite a single pool of non-selective inhibitory neurons (I). Bottom: classification accuracy of excitatory (blue) and inhibitory (red) neurons as a function of the relative strength of excitatory-to-inhibitory versus inhibitory-to-excitatory connections. Arrows in this and subsequent panels: parameter value in line with experimental data.

(B) Top: signal-selective model. $I_1$ and $I_2$, pools of inhibitory neurons connected more strongly to $E_1$ and $E_2$, respectively, than to $E_2$ and $E_1$; cross-pool connections are weaker than within-pool connections. Bottom: decoding accuracy of inhibitory and excitatory neurons match at the biologically plausible regime (arrow). Cross-pool connectivity was 25% smaller than within-pool connectivity.

(C) Top: SNR-selective model. Inhibitory neurons connect more strongly to excitatory neurons with high SNRs. Bottom: decoding accuracy of inhibitory and excitatory neurons match near the biologically plausible regime (arrow). All plots reflect 50 excitatory and 50 inhibitory neurons of a population containing 4,000 excitatory/1,000 inhibitory neurons.

To test this quantitatively, we modeled a non-selective circuit to evaluate the selectivity of inhibitory neurons (STAR Methods). Classification accuracy depended on the connection strengths between excitatory and inhibitory neurons (horizontal axis in Figure 5A, bottom) because those connection strengths affect overall activity in the network. The most biologically plausible regime is near 0, corresponding to equal strengths for excitatory-to-inhibitory and inhibitory-to-excitatory connections (Thomson and Lamy, 2007; Jouhanneau et al., 2015, 2018; Znamenskiy et al., 2018; Figure 5A, bottom, arrow). For this value (and indeed for all other values), inhibitory neurons had a lower classification accuracy than excitatory neurons (Figure 5A, bottom; Figure S8, left), inconsistent with our experimental results (Figures 3B and 3C). Therefore, in the non-selective circuit, although some inhibitory neurons are selective because of random biased inputs from the excitatory pools, the classification accuracy of inhibitory neurons will still be lower than that of excitatory neurons, regardless of the model parameters. This is because even modest amounts of noise in the system are sufficient to overcome any informative randomness in excitatory-to-inhibitory connections.

Next, we modeled a signal-selective circuit in which inhibitory neurons were connected preferentially to one excitatory pool (Figure 5B, top). In this circuit architecture, inhibitory and excitatory neurons had matched classification accuracy when the connection strength from excitatory to inhibitory neurons was about the same as the strength from inhibitory to excitatory ones (Figure 5B, bottom; Figure S8, center).

Interestingly, a third circuit configuration likewise gave rise to excitatory and inhibitory neurons with matched classification accuracy near the biologically plausible regime (Figure 5C, bottom; Figure S8, right). Here, inhibitory neurons were connected to excitatory neurons with a high signal-to-noise ratio (SNR) (Figure 5C, top).

Our modeling results raise two questions. First, how can the inhibitory population have a higher classification accuracy than the excitatory population (Figures 5B and 5C, bottom; for part of the plot, red is above blue), given that all information regarding the choice flows through the excitatory neurons? Second, why is the relative strength of the excitatory-to-inhibitory versus inhibitory-to-excitatory connections the critical parameter (Figure 5, bottom, x axis)? The answers are related. Increasing the strength of the excitatory-to-inhibitory connections increases the signal in the inhibitory neurons, effectively decreasing the noise added to the inhibitory population (see STAR Methods for details). This decrease in noise leads to improved decoding accuracy of both populations because they are connected. However, the decrease in the noise added to the inhibitory neurons has a bigger effect on the inhibitory than the excitatory population because the noise directly affects the inhibitory neurons but
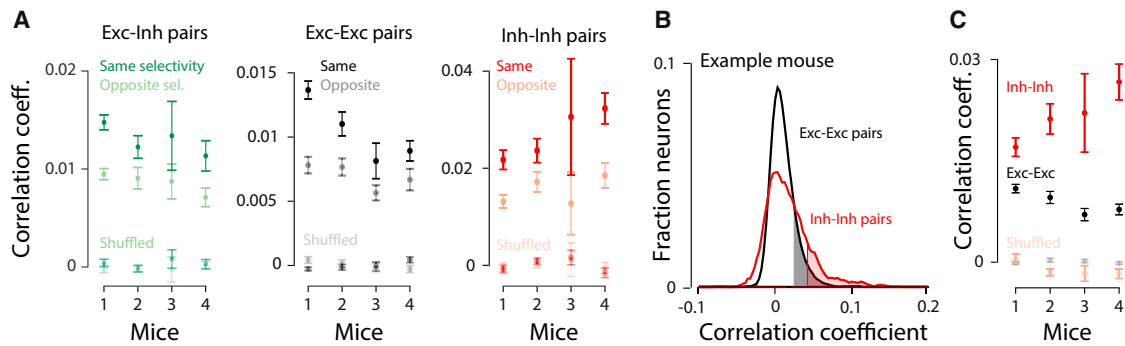
**Figure 6. Pairwise Noise Correlations Are Stronger between Neurons with the Same Choice Selectivity**
(A) Left: noise correlations (Pearson's coefficient) for pairs of excitatory-inhibitory neurons with the same (dark green) or opposite (light green) choice selectivity. Center and right: same as left, but for excitatory-excitatory and inhibitory-inhibitory pairs, respectively. "Shuffled" denotes that quantities were computed using shuffled trial labels. Mean ± SEM across days; 0–97 ms before the choice. Same versus opposite is significant in all cases, except for mouse 3 in excitatory-excitatory (EE) and inhibitory-inhibitory (II) pairs (t test, p < 0.05).
(B) Example mouse. Distribution of noise correlations (Pearson's correlation coefficients, 0–97 ms before the choice) for excitatory (blue, n = 11,867) and inhibitory (red, n = 15,83) neurons. Shaded areas, significance compared with a shuffled control in which trial orders were shuffled for each neuron to remove noise correlations.
(C) Summary of noise correlation coefficients; mean ± SEM across days.

affects the excitatory neurons only indirectly through the inhibitory-to-excitatory connections. Thus, in all panels of Figure 5, classification accuracy increases faster for inhibitory neurons than excitatory ones as the excitatory-to-inhibitory connection strength increases. Interestingly, the classification accuracy of both populations was overall higher for the signal-selective and SNR-selective models because the selective targeting in those models mitigates the noise that limits classification accuracy. This advantage was most pronounced for the signal-selective model; the model has a significantly higher classification accuracy compared with other models at all values of connectivity strength and noise (Figure S9). This may indicate that the signal-selective network configuration is especially advantageous for accurate decoding in the presence of noise.

Overall, the modeling rules out decision circuits with non-selective inhibition (Figure 5A) and instead demonstrates that excitatory and inhibitory neurons in decision circuits must be selectively connected, either based on the signal preference (Figure 5B) or the informativeness (Figure 5C) of excitatory neurons.

## Correlations Are Stronger between Similarly Tuned Neurons

If choice selectivity in inhibitory neurons emerges because of targeted input from excitatory neurons, then one prediction is that correlations will be stronger between excitatory and inhibitory neurons with the same choice selectivity compared with those with the opposite choice selectivity (Cossell et al., 2015; Francis et al., 2018). To test this hypothesis, we compared pairwise noise correlations in the activity of neurons with same versus opposite choice selectivity (STAR Methods). Indeed, neurons with the same choice selectivity had stronger correlations (Figure 6A), in keeping with previous observations in mouse V1 during passive viewing (Hofer et al., 2011; Ko et al., 2011; Cossell et al., 2015; Znamenskiy et al., 2018), as well as the prefrontal cortex in behaving monkeys (Constantinidis and Goldman-Rakic, 2002).

The higher noise correlations among similarly tuned excitatory-inhibitory neuron pairs is also consistent with the observation that, in V1, excitatory and inhibitory neurons that belong to the same subnetwork are reciprocally connected (Yoshimura and Callaway, 2005). An alternative explanation, that neurons with similar tuning share common inputs, is also possible. If that is the case, however, then the common input is not exclusively stimulus driven because we observed the same correlation effects in the pre-trial period, in which there is no stimulus (Figure S10A).

We next compared the strength of pairwise noise correlations within excitatory and inhibitory populations. Inhibitory pairs had significantly higher noise correlations compared with excitatory pairs (Figures 6B and 6C, noise correlations; Figure S10C, spontaneous correlations). This was true even when we restricted the analysis to inhibitory and excitatory neurons with the same inferred spiking activity (Figures S10D and S10E). Finally, similar to previous reports (Hofer et al., 2011; Khan et al., 2018), we found intermediate correlations for pairs consisting of one inhibitory neuron and one excitatory neuron (Figures S10B and S10C). Our findings align with previous studies in sensory areas reporting stronger correlations among inhibitory neurons (Hofer et al., 2011; Khan et al., 2018). The correlations are likely driven at least in part by local connections, as evidenced by the dense connectivity of interneurons with each other (Galarreta and Hestrin, 1999; Packer and Yuste, 2011; Kwan and Dan, 2012). The difference we observed between excitatory and inhibitory neurons argues that this feature of early sensory circuits is shared by decision-making areas. Further, this clear difference between excitatory and inhibitory neurons, like the difference in inferred spiking (Figures 1G–1I) and outcome selectivity (Figure S6C), confirms that we successfully measured two distinct populations. Overall, noise correlation analyses suggest that selective connectivity between excitatory and inhibitory neurons depends on their functional properties.
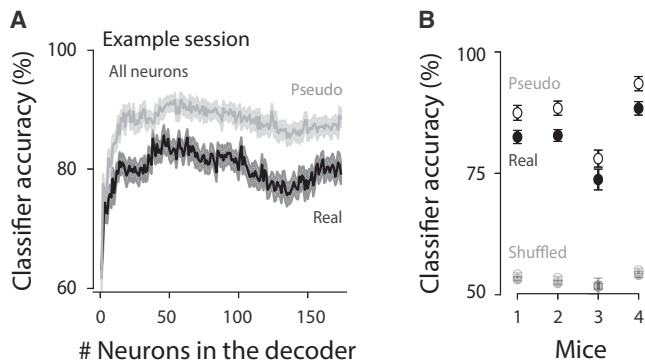
**Figure 7. Noise Correlations Reduce Classification Accuracy**
(A) Classification accuracy for an example session (0–97 ms before the choice) on neural ensembles of increasingly larger size. Mean ± SEM (50 cross-validated samples). Gray, classification accuracy for pseudo-populations; black, real populations. Both cell types were included ("All neurons").
(B) Summary for each mouse; points show mean ± SEM across days. Values were computed for the largest neuronal ensemble (the maximum value on the horizontal axis in A).

## Noise Correlations Limit Decoding Accuracy

Our results thus far demonstrate that neural activity in both excitatory and inhibitory populations reflect an animal's impending choice (Figures 3B and 3C) and that there are significant noise correlations among neurons in PPC (Figure 6). However, the analyses so far do not demonstrate how this noise affects the ability to decode neural activity. Examining the effect of noise is essential because correlations affect classifier performance (Panzeri et al., 1999; Averbeck et al., 2006), even when correlations are weak (Averbeck et al., 2006; Moreno-Bote et al., 2014). Fortunately, our dataset with simultaneous activity from hundreds of neurons is especially well suited to assess noise correlations.

To examine how noise correlations affect classification accuracy, we sorted neurons based on individual choice selectivity, adding them one by one to the population (from highest to lowest choice selectivity, defined as |AUC-0.5|). Classification accuracy improved initially as more neurons were included in the decoder but saturated quickly (Figure 7A, black).

To assess the effect of noise correlations on classification accuracy, we created "pseudopopulations" in which each neuron in the population was taken from a different trial (Figure 7A, gray). This removed noise correlations because those are shared across neurons within a single trial. A higher classification accuracy in pseudopopulations compared with real populations indicates the presence of noise that overlaps with signal, limiting information (Panzeri et al., 1999; Averbeck et al., 2006; Averbeck and Lee, 2006; Moreno-Bote et al., 2014). This is what we observed (Figure 7A, gray trace above black trace). In all mice, removing noise correlations resulted in a consistent increase in classification accuracy (Figure 7B; filled versus open circles), establishing that noise correlations limit population accuracy in the PPC.

## Selectivity Increases in Parallel in Inhibitory and Excitatory Populations during Learning

Our observations so far argue that excitatory and inhibitory neurons form selective subnetworks. To assess whether the emer-

gence of these subnetworks is experience dependent and whether it varies between inhibitory and excitatory populations, we measured neural activity as animals transitioned from novice to expert decision-makers (3 mice, 35–48 sessions; Figure S11). We trained a linear classifier for each training session and for each moment in the trial.

The classification accuracy of the choice decoder increased consistently as animals became experts in decision-making (Figure 8A, left; Figure 8D, black), leading to a strong correlation between classifier accuracy and mouse performance over training (Figure 8B, left). The choice signal also became more prompt, emerging progressively earlier in the trial as mice became experts. Initially, classification accuracy was high only after the choice (Figure 8A, black arrow). As the animals gained experience, high classification accuracy occurred progressively earlier in the trial, eventually long before the choice (Figure 8A, gray arrow). This resulted in a negative correlation between mouse performance and the onset of super-threshold decoding accuracy (Figures 8C, left, and 8E, black).

Importantly, the choice signal emerged at the same time in both populations, and its magnitude and timing were matched for the two cell types throughout learning (Figures 8A–8C, center and right, and 8D and 8E, blue and red). This was not due to the presence of more correct trials in later sessions; an improvement in classification accuracy was clear even when the number of correct trials was matched for each session (Figure S13C). These findings indicate that learning induces the simultaneous emergence of choice-specific subpopulations in excitatory and inhibitory cells in the PPC.

Notably, the animal's licking or running behavior could not explain the learning-induced changes in the magnitude of classification accuracy (Figure S12). The center-spout licks preceding left versus right choices were similar during the course of learning (Figure S12A) and did not differ on early versus late training days (Figure S12B). The similarity in lick movements for early versus late sessions contrasts the changes in classification accuracy for early versus late sessions (Figure 8). We also assessed running behavior during learning (Figures S12C and S12D). In some sessions, the running distance differed preceding left versus right choices (Figure S12C). Nonetheless, when we restricted our analysis to days on which the running distance was indistinguishable for the two choices (0–97 ms before the choice, t test, p > 0.05), classifiers could still accurately predict the choice (Figure S12D). These observations provide reassurance that population activity does not entirely reflect preparation of licking and running movements and argue instead that population activity reflects the animal's stimulus-informed choice.

Finally, we studied how correlations changed over training. Pairwise correlations in neural activity were higher early in training, when mice were novices, compared with late in training, when mice approached expert behavior (Figure 8F, unsaturated colors above saturated colors). This was observed for all combinations of neural pairs (Figure 8F). These findings agree with previous reports suggesting that learning results in reduced noise correlations (Gu et al., 2011; Jeanne et al., 2013; Khan et al., 2018; Ni et al., 2018), enhancing information in neural populations. To test whether the learning-induced increase in
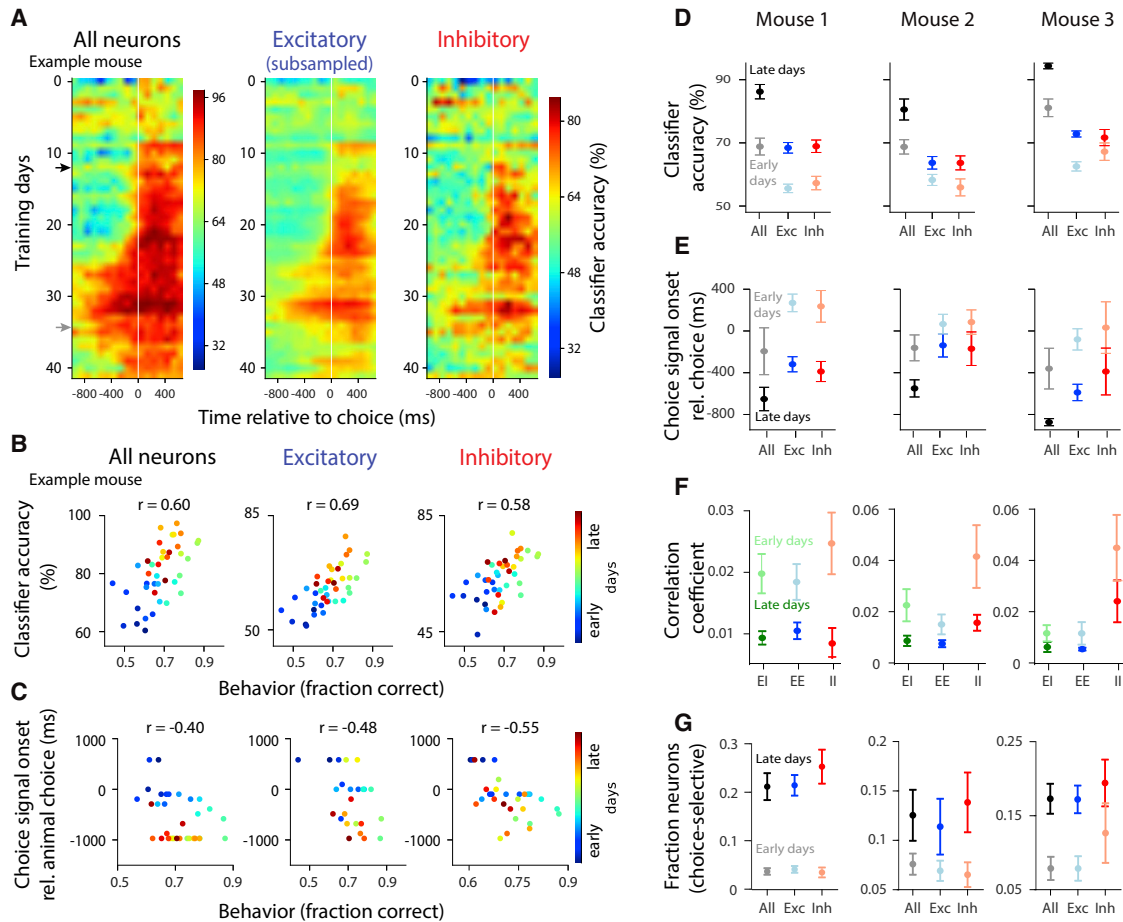
**Figure 8. Learning Leads to Improved Choice Decoding, an Increased Fraction of Choice-Selective Neurons, and Reduced Noise Correlations in Both Populations**

(A) Decoder accuracy for each training session for all neurons (left), subsampled excitatory neurons (center), and inhibitory neurons (right). White vertical line, choice; rows, average across cross-validated samples, example mouse. The color bar applies to both plots.

(B) Scatterplot of classifier accuracy (0–97 ms before choice) versus behavioral performance (fraction correct on easy trials) for all training days. r, Pearson correlation coefficient (p < 0.001 in all plots); same example mouse as in (A). Correlations for behavior versus classification accuracy for all neurons, excitatory and inhibitory: 0.55, 0.35, and 0.32 in mouse 2; 0.57, 0.63, and 0.32 in mouse 3. Correlations for behavior versus choice-signal onset for all neurons, excitatory and inhibitory: −0.60, −0.34, and −0.38 in mouse 2; −0.60, −0.27, and −0.28 in mouse 3. All values, p < 0.05.

(C) Same as (B) but showing the onset of choice signal (the first moment in the trial that classifier accuracy was above chance, relative to choice onset) versus behavioral performance.

(D) Summary of classification accuracy averaged across early (dim colors) versus late (dark colors) training days.

(E) Same as (D) but showing choice signal onset (milliseconds).

(F) Same as (D) but showing pairwise noise correlation coefficients. EI, excitatory-inhibitory.

(G) The fraction of choice-selective neurons increases over training; average across early (dim colors) and late (dark colors) training days (0–97 ms before the choice). Early days, first few training days on which the animal's performance was lower than the 20th percentile of performance across all days; late days, training days on which performance was above the 80th percentile of performance across all days.

classification accuracy (Figures 8A, 8B, and 8D) was entirely a consequence of the reduction in noise correlations (Figure 8F), we studied how the classification accuracy of pseudopopulations, which lack noise correlations, changed with training. Interestingly, a significant increase in the classification accuracy of pseudopopulations was present (Figures S13A and S13B). Therefore, the reduction in noise correlations cannot alone account for the improved classification accuracy during learning, suggesting that increased choice selectivity of individual neurons also contributes. Indeed, the fraction of choice-selective

neurons increased 3-fold during training in both excitatory and inhibitory neurons (Figure 8G).

## DISCUSSION

Despite a wealth of studies assessing the selectivity of inhibitory neurons for sensory features, little is known about the selectivity of inhibitory neurons in decision-making. This is a critical gap and has left untested key features of decision-making models relying on inhibitory neurons. To close this gap, we simultaneously

measured excitatory and inhibitory populations during perceptual decisions about multisensory stimuli.

We found that excitatory and inhibitory neurons predict the animal's impending choice with equal fidelity (Figures 2 and 3). This result, along with our modeling (Figure 5), constrains circuit models of decision-making, ruling out models in which inhibitory neurons receive completely nonspecific input from excitatory populations (Figure 5A). Instead, our findings suggest that specific functional subnetworks exist within inhibitory populations, just like in excitatory populations (Figure 5B). This implies targeted connectivity between excitatory and inhibitory neurons (Yoshimura and Callaway, 2005; Znamenskiy et al., 2018) and supports circuit architectures with functionally specific, reciprocally connected subnetworks.

A documented advantage of signal-selective architectures is that they can offer improved stability (Znamenskiy et al., 2018) and robustness to perturbations (Lim and Goldman, 2013). However, in our circuit, selectivity did not improve stability but instead improved performance; the classification accuracy for the signal-selective model was the highest of the three we tested (Figure 5B, bottom row; Figure S9). These observations raise the possibility that, among possible circuit architectures that could have been leveraged by the brain to support decision-making, the highest-performing one was chosen.

The equal selectivity for choice we observed in excitatory and inhibitory populations is perhaps, at first, surprising, given the broad stimulus tuning curves observed in most V1 inhibitory neurons (Sohya et al., 2007; Niell and Stryker, 2008; Kerlin et al., 2010; Bock et al., 2011; Hofer et al., 2011; Znamenskiy et al., 2018; but see Runyan et al., 2010) and the dense connectivity for inhibitory neurons (Hofer et al., 2011; Packer and Yuste, 2011; Znamenskiy et al., 2018). Two differences between our study and previous ones may explain why we saw equal selectivity in excitatory and inhibitory populations.

First, we measured neural activity in the PPC where the proportion of interneuron subtypes differs from V1; V1 is enriched for parvalbumin (PV) interneurons relative to somatostatin (SOM) and vasoactive intestinal polypeptide (VIP) neurons, whereas the opposite is true in association areas (Kim et al., 2017; Wang and Yang, 2018). Moreover, interneuron subtypes vary in their specificity of connections (Pfeffer et al., 2013); for instance, PV interneurons have broader tuning than SOM and VIP cells (Wang et al., 2004; Ma et al., 2010). Therefore, the strong selectivity we found in all GABAergic interneurons in the PPC may not contradict the broad selectivity observed in studies largely performed on PV interneurons in V1. Future studies that measure the selectivity of distinct interneuron populations during decision-making in V1 versus the PPC will be helpful. Here we measured all GABAergic interneurons instead of individual interneuron subtypes because of the technical challenge of reliably identifying more than two cell types in a single mouse and because of the importance of simultaneously measuring the activity of excitatory and inhibitory neurons within the same subject. Had we lacked within-mouse measurements, our ability to compare excitatory versus inhibitory neurons would have been compromised by mouse-to-mouse variability (note the matched selectivity of excitatory and inhibitory neurons within mice in Figure 3C despite overall variability across mice).

Second, analyzing neural activity in the context of decision-making naturally led us to make different comparisons than those carried out previously. For example, we measured selectivity for a binary choice, whereas sensory tuning curves are measured in response to continuously varying stimuli (e.g., orientation). Further, we measured activity in response to abstract stimuli, the meaning of which was learned gradually by the animal. This may recruit circuits that differ from those supporting sensory processing in passively viewing mice. Finally, we used stochastically fluctuating multisensory stimuli, which have not been evaluated in mouse V1. Future studies that examine the tuning of V1 neurons to the sensory stimulus used here will determine whether V1 inhibitory neurons will be as sharply tuned as excitatory neurons to the stimulus. This is a possibility; the tuning strength of interneurons can vary substantially for different stimulus features. For instance, PV neurons in V1 have particularly poor tuning to orientation, but their temporal-frequency tuning is considerably stronger (Znamenskiy et al., 2018).

We not only studied expert animals but also evaluated how acquiring expertise modulates activity. We observed that learning increased the number of choice-selective neurons and decreased noise correlations, indicating plasticity and reorganization of connections. Population responses preceding the two choices thus became progressively more distinct with training. Importantly, these changes occur in parallel in excitatory and inhibitory cells. Our findings are partially in agreement with those in V1, in which learning improves tuning to sensory stimuli in excitatory (Schoups et al., 2001; Poort et al., 2015; Khan et al., 2018) and some inhibitory (Khan et al., 2018) neurons. However, V1 excitatory neurons have stronger tuning to sensory stimuli early in training (Khan et al., 2018); in contrast, in our study, the magnitude of choice selectivity in the PPC was the same for both cell types throughout training (Figure 8). Primate studies have likewise observed that perceptual learning changes the selectivity of neurons (Freedman and Assad, 2006; Law and Gold, 2008; Viswanathan and Nieder, 2015) and reduces noise correlations (Gu et al., 2011; Ni et al., 2018).

Finally, we demonstrated that learning-induced changes in selectivity were closely associated with changes in animal performance, in keeping with primate studies of decision-making (Law and Gold, 2008). This, together with our finding that changes in population activity do not purely reflect movements (Figure S12), corroborates the suggested role of the PPC in mapping sensation to action (Law and Gold, 2008; Raposo et al., 2014; Pho et al., 2018). Future experiments using causal manipulations will reveal whether the increased choice selectivity we observed in the PPC originates there or is inherited from elsewhere in the brain.

By measuring cell-type-specific activity in the parietal cortex during decision-making, we observed that excitatory and inhibitory populations are equally choice selective and that these ensembles emerge in parallel as mice become skilled decision-makers. These results argue against models with non-specific connectivity between excitatory and inhibitory neurons, at least in decision circuits. Future modeling efforts can incorporate subnetworks and evaluate their effect on key model outputs, such as

reaction time distributions and firing rates. Such studies will shed light on how microcircuits of inhibitory and excitatory neurons vary across areas in their selectivity and specificity of connections and will reveal the circuit architectures that allow equally selective inhibitory and excitatory neurons.

## STAR★METHODS

Detailed methods are provided in the online version of this paper and include the following:

- KEY RESOURCES TABLE
- LEAD CONTACT AND MATERIALS AVAILABILITY
- EXPERIMENTAL MODEL AND SUBJECT DETAILS
- METHOD DETAILS
  - Surgical procedure
  - Imaging
  - Decision-making behavior
  - Logistic regression model of behavior
  - ROI (region of interest) extraction and deconvolution
  - Neuropil Contamination removal
  - ROI inclusion criteria
  - Identification of inhibitory neurons
  - ROC analysis
  - Decoding population activity
  - Stability
  - Noise correlations
  - Learning analysis
  - Modeling decision circuits
  - Connectivity matrices
  - Simulation details
  - Immunofluorescence staining for TdTomato and GABA
- QUANTIFICATION AND STATISTICAL ANALYSIS
- DATA AND CODE AVAILABILITY

### SUPPLEMENTAL INFORMATION

Supplemental Information can be found online at https://doi.org/10.1016/j.neuron.2019.09.045.

### AUTHOR CONTRIBUTIONS

Conceptualization and Writing, F.N. and A.K.C.; Experiments and Analysis, F.N.; Decoding Methodology and Common-Slope Regression Model, G.F.E., J.P.C., and F.N.; Circuit Modeling, R.C. and P.E.L.; Spike Inference Methodology, E.P.; Funding Acquisition, Resources, and Supervision, A.K.C.

### REFERENCES

Akrami, A., Kopec, C.D., Diamond, M.E., and Brody, C.D. (2018). Posterior parietal cortex represents sensory history and mediates its effects on behaviour. Nature 554, 368–372.

Allen, W.E., Kauvar, I.V., Chen, M.Z., Richman, E.B., Yang, S.J., Chan, K., Gradinaru, V., Deverman, B.E., Luo, L., and Deisseroth, K. (2017). Global Representations of Goal-Directed Behavior in Distinct Cell Types of Mouse Neocortex. Neuron 94, 891–907.e6.

Atallah, B.V., Bruns, W., Carandini, M., and Scanziani, M. (2012). Parvalbumin-expressing interneurons linearly transform cortical responses to visual stimuli. Neuron 73, 159–170.

Averbeck, B.B., and Lee, D. (2006). Effects of noise correlations on information encoding and decoding. J. Neurophysiol. 95, 3633–3644.

Averbeck, B.B., Latham, P.E., and Pouget, A. (2006). Neural correlations, population coding and computation. Nat. Rev. Neurosci. 7, 358–366.

Beaulieu, C. (1993). Numerical data on neocortical neurons in adult rat, with special reference to the GABA population. Brain Res. 609, 284–292.

Beck, J.M., Ma, W.J., Kiani, R., Hanks, T., Churchland, A.K., Roitman, J., Shadlen, M.N., Latham, P.E., and Pouget, A. (2008). Probabilistic population codes for Bayesian decision making. Neuron 60, 1142–1152.

Bock, D.D., Lee, W.C., Kerlin, A.M., Andermann, M.L., Hood, G., Wetzel, A.W., Yurgenson, S., Soucy, E.R., Kim, H.S., and Reid, R.C. (2011). Network anatomy and in vivo physiology of visual cortical neurons. Nature 471, 177–182.

Bogacz, R., Brown, E., Moehlis, J., Holmes, P., and Cohen, J.D. (2006). The physics of optimal decision making: a formal analysis of models of performance in two-alternative forced-choice tasks. Psychol. Rev. 113, 700–765.

Brunton, B.W., Botvinick, M.M., and Brody, C.D. (2013). Rats and humans can optimally accumulate evidence for decision-making. Science 340, 95–98.

Busse, L., Ayaz, A., Dhruv, N.T., Katzner, S., Saleem, A.B., Schölvinck, M.L., Zaharia, A.D., and Carandini, M. (2011). The detection of visual contrast in the behaving mouse. J. Neurosci. 31, 11351–11361.

Ch'ng, Y.H., and Reid, R.C. (2010). Cellular imaging of visual cortex reveals the spatial and functional organization of spontaneous activity. Front. Integr. Neurosci. 4, 20.

Chen, T.W., Wardill, T.J., Sun, Y., Pulver, S.R., Renninger, S.L., Baohan, A., Schreiter, E.R., Kerr, R.A., Orger, M.B., Jayaraman, V., et al. (2013). Ultrasensitive fluorescent proteins for imaging neuronal activity. Nature 499, 295–300.

Constantinidis, C., and Goldman-Rakic, P.S. (2002). Correlated discharges among putative pyramidal neurons and interneurons in the primate prefrontal cortex. J. Neurophysiol. 88, 3487–3497.

Cossell, L., Iacaruso, M.F., Muir, D.R., Houlton, R., Sader, E.N., Ko, H., Hofer, S.B., and Mrsic-Flogel, T.D. (2015). Functional organization of excitatory synaptic strength in primary visual cortex. Nature 518, 399–403.

de Lima, A.D., and Voigt, T. (1997). Identification of two distinct populations of gamma-aminobutyric acidergic neurons in cultures of the rat cerebral cortex. J. Comp. Neurol. 388, 526–540.

de Lima, A.D., Gieseler, A., and Voigt, T. (2009). Relationship between GABAergic interneurons migration and early neocortical network activity. Dev. Neurobiol. 69, 105–123.

Deneve, S., Latham, P.E., and Pouget, A. (1999). Reading population codes: a neural implementation of ideal observers. Nat. Neurosci. 2, 740–745.

Driscoll, L.N., Pettit, N.L., Minderer, M., Chettih, S.N., and Harvey, C.D. (2017). Dynamic Reorganization of Neuronal Activity Patterns in Parietal Cortex. Cell *170*, 986–999.e16.

Ego-Stengel, V., and Wilson, M.A. (2007). Spatial selectivity and theta phase precession in CA1 interneurons. Hippocampus *17*, 161–174.

Elsayed, G.F., Lara, A.H., Kaufman, M.T., Churchland, M.M., and Cunningham, J.P. (2016). Reorganization between preparatory and movement population responses in motor cortex. Nat. Commun. *7*, 13239.

Francis, N.A., Winkowski, D.E., Sheikhattar, A., Armengol, K., Babadi, B., and Kanold, P.O. (2018). Small Networks Encode Decision-Making in Primary Auditory Cortex. Neuron *97*, 885–897.e6.

Freedman, D.J., and Assad, J.A. (2006). Experience-dependent representation of visual categories in parietal cortex. Nature *443*, 85–88.

Funamizu, A., Kuhn, B., and Doya, K. (2016). Neural substrate of dynamic Bayesian inference in the cerebral cortex. Nat. Neurosci. *19*, 1682–1689.

Gabbott, P.L., Dickie, B.G., Vaid, R.R., Headlam, A.J., and Bacon, S.J. (1997). Local-circuit neurones in the medial prefrontal cortex (areas 25, 32 and 24b) in the rat: morphology and quantitative distribution. J. Comp. Neurol. *377*, 465–499.

Galarreta, M., and Hestrin, S. (1999). A network of fast-spiking cells in the neocortex connected by electrical synapses. Nature *402*, 72–75.

Giovannucci, A., Friedrich, J., Gunn, P., Kalfon, J., Brown, B.L., Koay, S.A., Taxidis, J., Najafi, F., Gauthier, J.L., Zhou, P., et al. (2019). CaImAn: An open source tool for scalable calcium imaging data analysis. eLife *8*, e38173.

Goard, M.J., Pho, G.N., Woodson, J., and Sur, M. (2016). Distinct roles of visual, parietal, and frontal motor cortices in memory-guided sensorimotor decisions. eLife *5*, e13764.

Green, D.M., and Swets, J.A. (1966). Signal detection theory and psychophysics (Wiley).

Gu, Y., Liu, S., Fetsch, C.R., Yang, Y., Fok, S., Sunkara, A., DeAngelis, G.C., and Angelaki, D.E. (2011). Perceptual learning reduces interneuronal correlations in macaque visual cortex. Neuron *71*, 750–761.

Guizar-Sicairos, M., Thurman, S.T., and Fienup, J.R. (2008). Efficient subpixel image registration algorithms. Opt. Lett. *33*, 156–158.

Harvey, C.D., Coen, P., and Tank, D.W. (2012). Choice-specific sequences in parietal cortex during a virtual-navigation decision task. Nature *484*, 62–68.

Helmchen, F., and Tank, D.W. (2019). A Single-Compartment Model of Calcium Dynamics in Nerve Terminals and Dendrites. Cold Spring Harb. Protoc. *2015*, 155–167.

Hofer, S.B., Ko, H., Pichler, B., Vogelstein, J., Ros, H., Zeng, H., Lein, E., Lesica, N.A., and Mrsic-Flogel, T.D. (2011). Differential connectivity and response dynamics of excitatory and inhibitory neurons in visual cortex. Nat. Neurosci. *14*, 1045–1052.

Hofmann, T., Scholkopf, B., and Smola, A.J. (2008). Kernel methods in machine learning. Ann. Stat. *36*, 1171–1220.

Hwang, E.J., Dahlen, J.E., Mukundan, M., and Komiyama, T. (2017). History-based action selection bias in posterior parietal cortex. Nat. Commun. *8*, 1242.

Isaacson, J.S., and Scanziani, M. (2011). How inhibition shapes cortical activity. Neuron *72*, 231–243.

Jeanne, J.M., Sharpee, T.O., and Gentner, T.Q. (2013). Associative learning enhances population coding by inverting interneuronal correlation patterns. Neuron *78*, 352–363.

Jouhanneau, J.S., Kremkow, J., Dorrn, A.L., and Poulet, J.F. (2015). In Vivo Monosynaptic Excitatory Transmission between Layer 2 Cortical Pyramidal Neurons. Cell Rep. *13*, 2098–2106.

Jouhanneau, J.S., Kremkow, J., and Poulet, J.F.A. (2018). Single synaptic inputs drive high-precision action potentials in parvalbumin expressing GABAergic cortical neurons in vivo. Nat. Commun. *9*, 1540.

Kamigaki, T., and Dan, Y. (2017). Delay activity of specific prefrontal interneuron subtypes modulates memory-guided behavior. Nat. Neurosci. *20*, 854–863.

Kerlin, A.M., Andermann, M.L., Berezovskii, V.K., and Reid, R.C. (2010). Broadly tuned response properties of diverse inhibitory neuron subtypes in mouse visual cortex. Neuron *67*, 858–871.

Khan, A.G., Poort, J., Chadwick, A., Blot, A., Sahani, M., Mrsic-Flogel, T.D., and Hofer, S.B. (2018). Distinct learning-induced changes in stimulus selectivity and interactions of GABAergic interneuron classes in visual cortex. Nat. Neurosci. *21*, 851–859.

Kim, Y., Yang, G.R., Pradhan, K., Venkataraju, K.U., Bota, M., Garcia Del Molino, L.C., Fitzgerald, G., Ram, K., He, M., Levine, J.M., et al. (2017). Brain-wide Maps Reveal Stereotyped Cell-Type-Based Cortical Architecture and Subcortical Sexual Dimorphism. Cell *171*, 456–469.e22.

Kimmel, D., Elsayed, G.F., Cunningham, J.P., Rangel, A., and Newsome, W.T. (2016). Encoding of value and choice as separable, dynamic neural dimensions in orbitofrontal cortex (Cosyne).

Ko, H., Hofer, S.B., Pichler, B., Buchanan, K.A., Sjöström, P.J., and Mrsic-Flogel, T.D. (2011). Functional specificity of local synaptic connections in neocortical networks. Nature *473*, 87–91.

Krishna, V.R., Alexander, K.R., and Peachey, N.S. (2002). Temporal properties of the mouse cone electroretinogram. J. Neurophysiol. *87*, 42–48.

Kwan, A.C., and Dan, Y. (2012). Dissection of cortical microcircuits by single-neuron stimulation in vivo. Curr. Biol. *22*, 1459–1467.

Law, C.T., and Gold, J.I. (2008). Neural correlates of perceptual learning in a sensory-motor, but not a sensory, cortical area. Nat. Neurosci. *11*, 505–513.

Lee, W.C., Bonin, V., Reed, M., Graham, B.J., Hood, G., Glattfelder, K., and Reid, R.C. (2016). Anatomy and function of an excitatory network in the visual cortex. Nature *532*, 370–374.

Lim, S., and Goldman, M.S. (2013). Balanced cortical microcircuitry for maintaining information in working memory. Nat. Neurosci. *16*, 1306–1314.

Liu, B.H., Li, P., Li, Y.T., Sun, Y.J., Yanagawa, Y., Obata, K., Zhang, L.I., and Tao, H.W. (2009). Visual receptive field structure of cortical inhibitory neurons revealed by two-photon imaging guided recording. J. Neurosci. *29*, 10520–10532.

Lo, C.C., and Wang, X.J. (2006). Cortico-basal ganglia circuit mechanism for a decision threshold in reaction time tasks. Nat. Neurosci. *9*, 956–963.

Lovett-Barron, M., Kaifosh, P., Kheirbek, M.A., Danielson, N., Zaremba, J.D., Reardon, T.R., Turi, G.F., Hen, R., Zemelman, B.V., and Losonczy, A. (2014). Dendritic inhibition in the hippocampus supports fear learning. Science *343*, 857–863.

Ma, W.P., Liu, B.H., Li, Y.T., Huang, Z.J., Zhang, L.I., and Tao, H.W. (2010). Visual representations by cortical somatostatin inhibitory neurons–selective but with weak and delayed responses. J. Neurosci. *30*, 14371–14379.

Machado, T.A., Pnevmatikakis, E., Paninski, L., Jessell, T.M., and Miri, A. (2015). Primacy of Flexor Locomotor Pattern Revealed by Ancestral Reversion of Motor Neuron Identity. Cell *162*, 338–350.

Machens, C.K., Romo, R., and Brody, C.D. (2005). Flexible control of mutual inhibition: a neural model of two-interval discrimination. Science *307*, 1121–1124.

Madisen, L., Zwingman, T.A., Sunkin, S.M., Oh, S.W., Zariwala, H.A., Gu, H., Ng, L.L., Palmiter, R.D., Hawrylycz, M.J., Jones, A.R., et al. (2010). A robust and high-throughput Cre reporting and characterization system for the whole mouse brain. Nat. Neurosci. *13*, 133–140.

Marbach, F., and Zador, A.M. (2017). A self-initiated two-alternative forced choice paradigm for head-fixed mice. bioRxiv. https://doi.org/10.1101/073783.

Maurer, A.P., Cowen, S.L., Burke, S.N., Barnes, C.A., and McNaughton, B.L. (2006). Phase precession in hippocampal interneurons showing strong functional coupling to individual pyramidal cells. J. Neurosci. *26*, 13485–13492.

Mi, Y., Katkov, M., and Tsodyks, M. (2017). Synaptic Correlates of Working Memory Capacity. Neuron *93*, 323–330.

Moore, A.K., and Wehr, M. (2013). Parvalbumin-expressing inhibitory interneurons in auditory cortex are well-tuned for frequency. J. Neurosci. *33*, 13713–13723.

Morcos, A.S., and Harvey, C.D. (2016). History-dependent variability in population dynamics during evidence accumulation in cortex. Nat. Neurosci. *19*, 1672–1681.

Moreno-Bote, R., Beck, J., Kanitscheider, I., Pitkow, X., Latham, P., and Pouget, A. (2014). Information-limiting correlations. Nat. Neurosci. *17*, 1410–1417.

Ni, A.M., Ruff, D.A., Alberts, J.J., Symmonds, J., and Cohen, M.R. (2018). Learning and attention reveal a general relationship between population activity and behavior. Science *359*, 463–465.

Niell, C.M., and Stryker, M.P. (2008). Highly selective receptive fields in mouse visual cortex. J. Neurosci. *28*, 7520–7536.

Odoemene, O., Pisupati, S., Nguyen, H., and Churchland, A.K. (2018). Visual evidence accumulation guides decision-making in unrestrained mice. J. Neurosci. *38*, 10143–10155.

Packer, A.M., and Yuste, R. (2011). Dense, unspecific connectivity of neocortical parvalbumin-positive interneurons: a canonical microcircuit for inhibition? J. Neurosci. *31*, 13260–13271.

Panzeri, S., Schultz, S.R., Treves, A., and Rolls, E.T. (1999). Correlations and the encoding of information in the nervous system. Proc. Biol. Sci. *266*, 1001–1012.

Pfeffer, C.K., Xue, M., He, M., Huang, Z.J., and Scanziani, M. (2013). Inhibition of inhibition in visual cortex: the logic of connections between molecularly distinct interneurons. Nat. Neurosci. *16*, 1068–1076.

Pho, G.N., Goard, M.J., Woodson, J., Crawford, B., and Sur, M. (2018). Task-dependent representations of stimulus and choice in mouse parietal cortex. Nat. Commun. *9*, 2596.

Pinto, L., and Dan, Y. (2015). Cell-Type-Specific Activity in Prefrontal Cortex during Goal-Directed Behavior. Neuron *87*, 437–450.

Pnevmatikakis, E.A., Soudry, D., Gao, Y., Machado, T.A., Merel, J., Pfau, D., Reardon, T., Mu, Y., Lacefield, C., Yang, W., et al. (2016). Simultaneous Denoising, Deconvolution, and Demixing of Calcium Imaging Data. Neuron *89*, 285–299.

Poort, J., Khan, A.G., Pachitariu, M., Nemri, A., Orsolic, I., Krupic, J., Bauza, M., Sahani, M., Keller, G.B., Mrsic-Flogel, T.D., and Hofer, S.B. (2015). Learning Enhances Sensory and Multiple Non-sensory Representations in Primary Visual Cortex. Neuron *86*, 1478–1490.

Raposo, D., Kaufman, M.T., and Churchland, A.K. (2014). A category-free neural population supports evolving demands during decision-making. Nat. Neurosci. *17*, 1784–1792.

Ringach, D.L., Mineault, P.J., Tring, E., Olivas, N.D., Garcia-Junco-Clemente, P., and Trachtenberg, J.T. (2016). Spatial clustering of tuning in mouse primary visual cortex. Nat. Commun. *7*, 12270.

Rübel, O., Tritt, A., Dichter, B., Braun, T., Cain, N., Clack, N., Davidson, T.J., Dougherty, M., Fillion-Robin, J.C., Graddis, N., et al. (2019). NWB:N 2.0: An Accessible Data Standard for Neurophysiology. bioRxiv. https://doi.org/10.1101/523035.

Rudy, B., Fishell, G., Lee, S., and Hjerling-Leffler, J. (2011). Three groups of interneurons account for nearly 100% of neocortical GABAergic neurons. Dev. Neurobiol. *71*, 45–61.

Runyan, C.A., Schummers, J., Van Wart, A., Kuhlman, S.J., Wilson, N.R., Huang, Z.J., and Sur, M. (2010). Response features of parvalbumin-expressing interneurons suggest precise roles for subtypes of inhibition in visual cortex. Neuron *67*, 847–857.

Runyan, C.A., Piasini, E., Panzeri, S., and Harvey, C.D. (2017). Distinct time-scales of population coding across cortex. Nature *548*, 92–96.

Rustichini, A., and Padoa-Schioppa, C. (2015). A neuro-computational model of economic decisions. J. Neurophysiol. *114*, 1382–1398.

Sahara, S., Yanagawa, Y., O'Leary, D.D., and Stevens, C.F. (2012). The fraction of cortical GABAergic neurons is constant from near the start of cortical neurogenesis to adulthood. J. Neurosci. *32*, 4755–4761.

Schoups, A., Vogels, R., Qian, N., and Orban, G. (2001). Practising orientation identification improves orientation coding in V1 neurons. Nature *412*, 549–553.

Sohya, K., Kameyama, K., Yanagawa, Y., Obata, K., and Tsumoto, T. (2007). GABAergic neurons are less selective to stimulus orientation than excitatory neurons in layer II/III of visual cortex, as revealed by in vivo functional Ca2+ imaging in transgenic mice. J. Neurosci. *27*, 2145–2149.

Song, Y.H., Kim, J.H., Jeong, H.W., Choi, I., Jeong, D., Kim, K., and Lee, S.H. (2017). A Neural Circuit for Auditory Dominance over Visual Perception. Neuron *93*, 940–954.e6.

Taniguchi, H., He, M., Wu, P., Kim, S., Paik, R., Sugino, K., Kvitsiani, D., Fu, Y., Lu, J., Lin, Y., et al. (2011). A resource of Cre driver lines for genetic targeting of GABAergic neurons in cerebral cortex. Neuron *71*, 995–1013.

Tanimoto, N., Sothilingam, V., Kondo, M., Biel, M., Humphries, P., and Seeliger, M.W. (2015). Electroretinographic assessment of rod- and cone-mediated bipolar cell pathways using flicker stimuli in mice. Sci. Rep. *5*, 10731.

Teeters, J.L., Godfrey, K., Young, R., Dang, C., Friedsam, C., Wark, B., Asari, H., Peron, S., Li, N., Peyrache, A., et al. (2015). Neurodata Without Borders: Creating a Common Data Format for Neurophysiology. Neuron *88*, 629–634.

Thomson, A.M., and Lamy, C. (2007). Functional maps of neocortical local circuitry. Front. Neurosci. *1*, 19–42.

Viswanathan, P., and Nieder, A. (2015). Differential impact of behavioral relevance on quantity coding in primate frontal and parietal neurons. Curr. Biol. *25*, 1259–1269.

Vogelstein, J.T., Packer, A.M., Machado, T.A., Sippy, T., Babadi, B., Yuste, R., and Paninski, L. (2010). Fast nonnegative deconvolution for spike train inference from population calcium imaging. J. Neurophysiol. *104*, 3691–3704.

Wang, X.J. (2002). Probabilistic decision making by slow reverberation in cortical circuits. Neuron *36*, 955–968.

Wang, X.J., and Yang, G.R. (2018). A disinhibitory circuit motif and flexible information routing in the brain. Curr. Opin. Neurobiol. *49*, 75–83.

Wang, X.J., Tegnér, J., Constantinidis, C., and Goldman-Rakic, P.S. (2004). Division of labor among distinct subtypes of inhibitory neurons in a cortical microcircuit of working memory. Proc. Natl. Acad. Sci. USA *101*, 1368–1373.

Wong, K.F., and Wang, X.J. (2006). A recurrent network mechanism of time integration in perceptual decisions. J. Neurosci. *26*, 1314–1328.

Yoshimura, Y., and Callaway, E.M. (2005). Fine-scale specificity of cortical networks depends on inhibitory cell type and connectivity. Nat. Neurosci. *8*, 1552–1559.

Yoshimura, Y., Dantzker, J.L., and Callaway, E.M. (2005). Excitatory cortical neurons form fine-scale functional networks. Nature *433*, 868–873.

Zhong, L., Zhang, Y., Duan, C.A., Pan, J., and Xu, N.-l. (2019). Dynamic and causal contribution of parietal circuits to perceptual decisions during category learning. Nat. Neurosci. *22*, 963–973.

Znamenskiy, P., Kim, M.-H., Muir, D.R., Iacaruso, M.F., Hofer, S.B., and Mrsic-Flogel, T.D. (2018). Functional selectivity and specific connectivity of inhibitory neurons in primary visual cortex. bioRxiv. https://doi.org/10.1101/294835.

# STAR★METHODS

## KEY RESOURCES TABLE

| REAGENT or RESOURCE | SOURCE | IDENTIFIER |
|---|---|---|
| Bacterial and Virus Strains | | |
| AAV9-Synapsin-GCaMP6f | U Penn, Vector Core Facility | N/A |
| Experimental Models: Organisms/Strains | | |
| Gad2-IRES-CRE | The Jackson Laboratory | 010802 |
| Rosa-CAG-LSL-tdTomato-WPRE | The Jackson Laboratory | 007914 |
| Software and Algorithms | | |
| CalmAn: computational toolbox for large scale Calcium Imaging Analysis | https://github.com/flatironinstitute/CalmAn | N/A |

## LEAD CONTACT AND MATERIALS AVAILABILITY

Further information and requests for resources should be directed to and will be fulfilled by the Lead Contact, Anne K. Churchland (churchland@cshl.edu). This study did not generate new unique reagents.

## EXPERIMENTAL MODEL AND SUBJECT DETAILS

Gad2-IRES-CRE (Taniguchi et al., 2011) mice were crossed with Rosa-CAG-LSL-tdTomato-WPRE (aka Ai14; Madisen et al., 2010) to create mice in which all GABAergic inhibitory neurons were labeled. Adult mice (∼2-month old; female and male) were used in the experiments.

## METHOD DETAILS

### Surgical procedure

Meloxicam (analgesic), dexamethasone (anti-inflammatory) and Baytril (enrofloxacin; anti-biotic) were injected 30min before surgery. Using a biopsy punch, a circular craniotomy (diameter: 3mm) was made over the left PPC (stereotaxic coordinates: 2 mm posterior, 1.7 mm lateral of bregma (Harvey et al., 2012) under isoflurane (∼5%) anesthesia. Pipettes (10-20 um in diameter, cut at an angle to provide a beveled tip) were front-filled with AAV9-Synapsin-GCaMP6f (U Penn, Vector Core Facility) diluted 2X in PBS (Phosphae-buffered saline). The pipette was slowly advanced into the brain (Narishige MO-8 hydraulic micro-manipulator) to make ∼3 injections of 50nL, slowly over an interval of ∼5-10 min, by applying air pressure using a syringe. Injections were made near the center of craniotomy at a depth of 250-350 μm below the dura. A glass plug consisting of a 5mm coverslip attached to a 3mm coverslip (using IR-curable optical bond, Norland) was used to cover the craniotomy window. Vetbond, followed by metabond, was used to seal the window. All surgical and behavioral procedures conformed to the guidelines established by the National Institutes of Health and were approved by the Institutional Animal Care and Use Committee of Cold Spring Harbor Laboratory.

### Imaging

We used a 2-photon Moveable Objective Microscope with resonant scanning at approximately 30 frames per second (Sutter Instruments, San Francisco, CA). A 16X, 0.8 NA Nikon objective lens was used to focus light on fields of view of size 512x512 pixels (∼575 μm x ∼575 μm). A Ti:sapphire laser (Coherent) delivered excitation light at 930nm (average power: 20-70 mW). Red (ET670/50 m) and green (ET 525/50 m) filters (Chroma Technologies) were used to collect red and green emission light. The microscope was controlled by Mscan (Sutter). In mice in which chronic imaging was performed during learning, the same plane was identified on consecutive days using both coarse alignment, based on superficial blood vessels, as well as fine alignment, using reference images of the red channel (tdTomato expression channel) at multiple magnification levels. For each trial, imaging was started 500ms before the trial-initiation tone, and continued 500ms after reward or time-out. We aimed to image in the center of the window for all mice, but in one animal (Mouse 4), some tissue regrowth obscured the signal in this region and so imaging was performed slightly further back.

### Decision-making behavior

Mice were gradually water restricted over the course of a week, and were weighed daily. Mice harvested at least 1 mL of water per behavioral/imaging session, and completed 100-500 trials per session. After approximately one week of habituation to the behavioral

setup, 15-30 training days were required to achieve 75% correct choice. Animal training took place in a sound isolation chamber. The stimulus in all trials was multisensory, consisting of a series of simultaneous auditory clicks and visual flashes, occurring with Poisson statistics (Brunton et al., 2013; Odoemene et al., 2018). Multisensory stimuli were selected because they increased the learning rate of the mice, a critical consideration since GCaMP6f expression can be unreliable over a long period of time. Stimulus duration was 1000 ms. Each pulse was 5 ms; minimum interval between pulses was 32 ms, and maximum interval was 250 ms. The pulse rate ranged from 5 to 27 Hz. The category boundary for marking high-rate and low-rate stimuli was 16 Hz, at which animals were rewarded randomly on either side. The highest stimulus rates used here are known to elicit reliable, steady state flicker responses in retinal ERG in mice (Krishna et al., 2002; Tanimoto et al., 2015).

Mice were on top of a cylindrical wheel and a rotary encoder was used to measure their running speed. Trials started with a 50 ms initiation tone (Figure S1A). Mice had 5 s to initiate a trial by licking the center waterspout (Marbach and Zador, 2017), after which the multisensory stimulus was played for 1 s. If mice again licked the center waterspout, they received 0.5 μL water on the center spout, and a 50ms go cue was immediately played. Animals had to report a choice by licking to the left or right waterspout within 2 s. Mice were required to confirm their choice by licking the same waterspout one more time within 300 ms after the initial lick (Marbach and Zador, 2017). The "confirmation lick" helped dissociate the choice time (i.e., the time of first lick to the side waterspout), from the reward time (i.e., the time of second lick to the side waterspout); it also helped with reducing impulsive choices. If the choice was correct, mice received 2-4 μL water on the corresponding waterspout. An incorrect choice was punished with a 2 s time-out. The experimenter-imposed inter-trial intervals (ITIs) were drawn from a truncated exponential distribution, with minimum, maximum, and lambda equal to 1 s, 5 s, and 0.3 s, respectively. However, the actual ITIs could be much longer depending on when the animal initiates the next trial. Bcontrol (Raposo et al., 2014) with a MATLAB interface was used to deliver trial events (stimulus, reward, etc) and collect data.

### Logistic regression model of behavior

A modified version of a logistic regression model in (Busse et al., 2011) was used to assess the extent to which the animal's choice depends on the strength of sensory evidence (how far the stimulus rate is from the category boundary at 16Hz), the previous choice outcome (success or failure) and ITI, (the time interval between the previous choice and the current stimulus onset) (Figure S1B). The model has the form

$$p = \frac{1}{1 + e^{-z}} \qquad \text{eq. 1}$$

$$z = \beta_0 + (\beta_{r1}R_1 + \beta_{r2}R_2 + \beta_{r3}R_3 + \beta_{r4}R_4 + \beta_{r5}R_5 + \beta_{r6}R_6) + (\beta_{s1}S_1 + \beta_{s2}S_2) + (\beta_{f1}F_1 + \beta_{f2}F_2)$$

where $p$ is the probability of choosing left. Stimulus strength ($R$) was divided into 6 bins ($R_1$ to $R_6$). Previous success ($S$) was divided into 2 bins ($S_1$ to $S_2$), with $S_1$ referring to success after a long ITI (> 7sec) and $S_2$ to success after a short ITI (< 7sec). Previous failure ($F$) was divided into 2 bins ($F_1$ to $F_2$), with $F_1$ referring to failure after a long ITI and $F_2$ to failure after a short ITI. For example, if a trial had stimulus strength 3 Hz, and was preceded by a success choice with ITI 5 s, then $R_2$ and $S_1$ would be set to 1 and all other R, S and F parameters to 0 (Figure S1B).

For each session the scalar coefficients $\beta_0$, $\beta_{r1}$ to $\beta_{r6}$, $\beta_{s1}$, $\beta_{s2}$, $\beta_{f1}$, and $\beta_{f2}$ were fit using MATLAB glmfit.m. Figure S1B left shows $\beta_{r1}$ to $\beta_{r6}$. Figure S1B middle shows $\beta_{s1}$ and $\beta_{s2}$, and Figure S1B right shows $\beta_{f1}$ and $\beta_{f2}$.

### ROI (region of interest) extraction and deconvolution

The recorded movies from all trials were concatenated and corrected for motion artifacts by cross-correlation using Discrete Fourier Transform (DFT) registration (Guizar-Sicairos et al., 2008). Subsequently, active ROIs (sources) were extracted using the Constrained Nonnegative Matrix Factorization (CNMF) algorithm (Pnevmatikakis et al., 2016) as implemented in the CaImAn package (Giovannucci et al., 2019) in MATLAB. The traces of the identified neurons were ΔF/F normalized and then deconvolved by adapting the FOOPSI deconvolution algorithm (Vogelstein et al., 2010; Pnevmatikakis et al., 2016) to a multi-trial setup. This was necessary because simply concatenating individual trials would lead to discontinuities in the traces, which could distort estimates of the time constants. Each value of Foopsi deconvolution represents spiking activity at each frame for a given neuron. We have referred to the deconvolved values as "inferred spiking activity" throughout the paper. The deconvolved values do not represent absolute firing rates, so they cannot be compared across neurons. However, for a particular neuron, higher inferred spiking activity means higher firing rate. We elected to base our analyses on inferred spiking activity rather than fluorescence activity because peak amplitudes and time constants of the fluorescence responses vary across neurons, affecting subsequent analyses (Machado et al., 2015; Helmchen and Tank, 2019).

We adapted the FOOPSI for multi-trial setup as follows. For each component, the activity trace over all the trials was used to determine the time constants of the calcium indicator dynamics as in (Pnevmatikakis et al., 2016). Then the neural activity during each trial was deconvolved separately using the estimated time constant and a zero baseline (since the traces were ΔF/F normalized). A difference of exponentials was used to simulate the rise and decay of the indicator.

### Neuropil Contamination removal

The CNMF algorithm demixes the activity of overlapping neurons. It takes into account background neuropil activity by modeling it as a low rank spatiotemporal matrix (Pnevmatikakis et al., 2016). In this study a rank two matrix was used to capture the neuropil activity. To evaluate its efficacy, we compared the traces obtained from CNMF to the traces from a "manual" method similar to (Chen et al., 2013; Figure S14): the set of spatial footprints (shapes) extracted from CNMF were binarized by thresholding each component at 20% of its maximum. The binary masks were then used to average the raw data and obtain an activity trace that also included neuropil effects. To estimate the background signal, an annulus around the binary mask was constructed with minimum distance 3 pixels from the binary mask and width 7 pixels (Figure S14A). The average of the raw data over the annulus defined the background trace, which was subtracted from the activity trace. The resulting trace was then compared with the CNMF estimated temporal trace for this activity. The comparison showed a very high degree of similarity between the two traces (Figure S14; example component; r = 0.96), with the differences between the components being attributed to noise and not neuropil related events. Note that this "manual" approach is only applicable in the case when the annulus does not overlap with any other detected sources. These results demonstrate the ability of the CNMF framework to properly capture neuropil contamination and remove it from the calcium traces.

### ROI inclusion criteria

We excluded poor-quality ROIs identified by the CNMF algorithm based on a combination of criteria: 1) size of the spatial component, 2) decay time constant, 3) correlation of the spatial component with the raw ROI image built by averaging spiking frames, 4) correlation of the temporal component with the raw activity trace, and 5) the probability of fluorescence traces maintaining values above an estimated signal-to-noise level for the expected duration of a calcium transient(Giovannucci et al., 2019) (GCaMP6f, frame rate: 30Hz). A final manual inspection was performed on the selected ROIs to validate their shape and trace quality.

### Identification of inhibitory neurons

We used a two-step method to identify inhibitory neurons. First, we corrected for bleed-through from green to red channel by considering the following regression model,

$$r_i(t) = \beta_i 1_p + s g_i(t) + \epsilon \qquad \text{(Equation 2)}$$

where, $r_i(t)$ and $g_i(t)$ are vectors, indicating pixel intensity in red and green channel, respectively, with each component of the vector corresponding to one pixel in the ROI, $i$ labels ROI (presumably each ROI is a neuron), $\beta_i$ is the offset, $1_p$ is a vector whose components are all 1, and $s$ is the parameter that tells us how much of the green channel bleeds through to the red one.

It is the parameter $s$ that we are interested in. To find $s$, we define a cost function, $C$,

$$C = \int dt \sum_i \left| r_i(t) - \beta_i 1_p + s g_i(t) \right|^2 \qquad \text{(Equation 3)}$$

and minimize it with respect to $s$ and all the $\beta_i$. The value of $s$ at the minimum reflects the fraction of bleed-through from the green to the red channel. That value, denoted $s^*$, is then used to compute the bleedthrough-corrected image of the red-channel, denoted $I$ via the expression

$$I = R - s^* G \qquad \text{(Equation 4)}$$

where $R$ and $G$ are the time-averaged images of the red and green channels, respectively.

Once the bleedthrough-corrected image, $I$, was computed, we used it to identify inhibitory neurons using two measures,

1) A measure of local contrast, by computing, on the red channel ($I$, Equation 4), the average pixel intensity inside each ROI mask relative to its immediate surrounding mask (width = 3 pixels). Given the distribution of contrast levels, we used two threshold levels, $T_E$ and $T_I$, defined, respectively, as the 80th and 90th percentiles of the local contrast measures of all ROIs. ROIs whose contrast measure fell above $T_I$ were identified as inhibitory neurons. ROIs whose contrast measure fell below $T_E$ were identified as excitatory neurons, and ROIs with the contrast measure in between $T_E$ and $T_I$ were not classified as either group ("unsure" class).

2) In addition to a measure of local contrast, we computed for each ROI the correlation between the spatial component (ROI image on the green channel) and the corresponding area on the red channel. High correlation values indicate that the ROI on the green channel has a high signal on the red channel too; hence the ROI is an inhibitory neuron. We used this correlation measure to further refine the neuron classes computed from the local contrast measure (i.e., measure 1 above). ROIs that were identified as inhibitory based on their local contrast (measure 1) but had low red-green channel correlation (measure 2), were reset as "unsure" neurons. Similarly, ROIs that were classified as excitatory (based on their local contrast) but had high red-green channel correlation were reclassified as unsure. Unsure ROIs were included in the analysis of all-neuron populations (Figure 3A left); but were excluded from the analysis of excitatory only or inhibitory only populations (Figure 3A middle, right). Finally, we manually inspected the ROIs identified as inhibitory to confirm their validity. This method resulted in 11% inhibitory neurons, which is within the range of previous studies (10%–20%: Rudy et al., 2011); (15%: Beaulieu, 1993); (16%: Gabbott et al., 1997); (< 5%: de Lima and Voigt, 1997); (10%–25%: de Lima et al., 2009).

### ROC analysis

The area under the ROC curve (AUC) was used to measure the choice preference of single neurons. Choice selectivity was defined as the absolute deviation of AUC from chance level: choice selectivity = 2*|AUC-0.5|. To identify significantly choice-selective neurons, for each neuron we performed ROC on shuffled trial labels (i.e., left and right choices were randomly assigned to each trial). This procedure was repeated 50 times to create a distribution of shuffled AUC values for each neuron (Figure S3A, "shuffled"). A neuron's choice selectivity was considered to be significant if the probability of the actual AUC (Figure S3A, "real") being drawn from the shuffled AUC distribution was less than 0.05. Time points from 0–97 ms before the decision were used to compute the fraction of choice-selective neurons (Figures 2B and 8G).

### Decoding population activity

A linear SVM (Python sklearn package) was trained on each bin of the population activity in each session (non-overlapping 97ms time bins). To break any dependencies on the sequence of trials, we shuffled the order of trials for the entire population. To avoid bias in favor of one choice over the other, we matched the number of left- and right-choice trials used for classifier training. L2 regularization was used to avoid over-fitting. 10-fold cross validation was performed by leaving out a random 10% subset of trials to test the classifier performance, and using the remaining trials for training the classifier. This procedure was repeated 50 times. A range of regularization values was tested, and the one that gave the smallest error on the validation dataset was chosen as the optimal regularization parameter. Classifier accuracy was computed as the percentage of testing trials in which the animal's choice was accurately predicted by the classifier, and summarized as the average across the 50 repetitions of trial subsampling. A minimum of 10 correct trials per choice was required in order to run the SVM on a session. Inferred spiking activity of each neuron was z-scored before running the SVM.

When comparing classification accuracy for excitatory versus inhibitory neurons, the excitatory population was randomly sub-sampled to match the population size of inhibitory neurons to enable a fair comparison (Figure 3, blue versus red). To compare the distribution of weights in the all-neuron classifier (Figure 3 black), the weight vector for each session was normalized to unity length (Figures 3D–3F).

When decoding the stimulus category (Figure S6B), we used stimulus-aligned trials, and avoided any contamination by the choice signal by sub-selecting equal number of left and right choice trials for each stimulus category. When decoding trial outcome (Figure S6C), we used outcome-aligned trials, and avoided contamination by the choice or stimulus signal by subselecting equal number of trials from left and right choice trials for each trial outcome.

### Stability

To test the stability of the population code, decoders were trained and tested at different time bins (Kimmel et al., 2016; Figure 4). To avoid the potential effects of auto-correlation, we performed cross validation not only across time bins, but also across trials. In other words, even though the procedure was cross validated by testing the classifier at a time different from the training time, we added another level of cross-validation by testing on a subset of trials that were not used for training. This strict method allowed our measure of stability duration to be free of auto-correlation effects.

As an alternative measure of stability, the angle between pairs of classifiers that were trained at different moments in the trial was computed (Figure S7C). Small angles indicate alignment, hence stability, of the classifiers. Large angles indicate misalignment, i.e., instability of the classifiers.

### Noise correlations

To estimate noise correlations, the order of trials was shuffled for each neuron independently. Shuffling was done within the trials of each choice, hence retaining the choice signal, while de-correlating the population activity to remove noise correlations. Then we classified population activity in advance of left versus right choice (at time bin 0–97 ms before the choice) using the de-correlated population activity. This procedure was performed on neural ensembles of increasingly larger size, with the most selective neurons (the ones with the largest value of |AUC-0.5|) added first (Figure 7A). To summarize how noise correlations affected classification accuracy in the population (Figure 7B), we computed, for the largest neural ensemble (Figure 7A, max value on the horizontal axis), the change in classifier accuracy in the de-correlated data ("pseudo populations") versus the original data. This analysis was only performed for the entire population; the small number of inhibitory neurons in each session prevented a meaningful comparison of classification accuracy on real versus pseudo populations.

To measure pairwise noise correlations, we subtracted the trial-averaged response to a particular choice from the response of single trials of that choice. This allowed removing the effect of choice on neural responses. The remaining variability in trial-by-trial responses can be attributed to noise correlations, measured as the Pearson correlation coefficient for neuron pairs. We also measured noise correlations using the spontaneous activity defined as the neural responses in 0-97 ms preceding the trial initiation tone (Figures S10A and S10C). We computed the pairwise correlation coefficient (Pearson) for a given neuron with each other neuron within an ensemble (e.g., excitatory neurons). The resulting coefficients were then averaged to generate a single correlation value for that neuron. This was repeated for all neurons within the ensemble (Figure 6).

To compute pairwise correlations on excitatory and inhibitory neurons with the same inferred spiking activity (Figures S10D and S10E), we computed the median inferred spiking activity across trials for individual excitatory and inhibitory neurons in a session.

The medians were then divided into 50 bins. The firing-rate bin that included the maximum number of inhibitory neurons was identified ("max bin"); inhibitory and excitatory neurons whose firing rate was within this "max bin" were used for the analysis. The firing rates were matched for these neurons because their median firing rate was within the same small bin of firing rates. Pairwise correlations were then computed as above.

### Learning analysis

In 3 of the mice, the same field of view was imaged each session during learning. This was achieved in two ways. First, the vasculature allowed a coarse alignment of the imaging location from day to day. Second, the image from the red channel was used for a finer alignment. Overall, most neurons were stably present across sessions (Figure S11). This suggests that we likely measured activity from a very similar population each day. Importantly, however, our conclusions do not rely on this assumption: our measures and findings focus on learning-related changes in the PPC population overall, as opposed to tracking changes in single neurons. To assess how population activity changed over learning, we evaluated classification accuracy each day, training a new decoder for each session. This approach allowed us to compute the best decoding accuracy for each session.

"Early days" (Figure 8; Figures S12 and S13) included the initial training days in which the animal's performance, defined as the fraction of correct choices on easy trials, was lower than the 20th percentile of performance across all days. "Late days" (Figure 8; Figures S12 and S13) included the last training days in which the animal's behavioral performance was above the 80th percentile of performance across all days.

To measure the timing of decision-related activity (Figures 8C and 8E), we identified all sessions in which classifier accuracy was significantly different than the shuffle (t test, p < 0.05) over a window of significance that was at least 500 ms long. We defined the "choice signal onset" (Figures 8C and 8E) as the trial time corresponding to the first moment of that window. Sessions in which the 500 ms window of significance was present are included in Figure 8C. The number of points (and hence the relationship between session number and color in Figure 8C) differs slightly across the three groups. This is because on some sessions, the window of significance was present in one group but not another. For example, in a session the population including all neurons might have a 500 ms window of significance, hence it will contribute a point to Figure 7C left, while the population with only inhibitory neurons might be only transiently significant for < 500ms, hence it will be absent from Figure 8C right.

### Modeling decision circuits

We considered a linearized rate network of the form

$$\frac{d\mathbf{v}_E}{dt} = -\mathbf{v}_E + \mathbf{W}_{EE} \cdot \mathbf{v}_E - \mathbf{W}_{EI} \cdot \mathbf{v}_I + \mathbf{h}_s + \xi_E$$

$$\frac{d\mathbf{v}_I}{dt} = -\mathbf{v}_I + \mathbf{W}_{IE} \cdot \mathbf{v}_E - \mathbf{W}_{II} \cdot \mathbf{v}_I + \xi_I$$

where $E$ and $I$ refer to the excitatory and inhibitory populations, respectively, $\mathbf{v}_E$ and $\mathbf{v}_I$ are vectors of firing rates ($\mathbf{v}_E = v_{E1}, v_{E2}, \ldots$, and similarly for $\mathbf{v}_I$), $\mathbf{W}_{EE}$, $\mathbf{W}_{EI}$, $\mathbf{W}_{IE}$ and $\mathbf{W}_{II}$ are the connectivity matrices ($\mathbf{W}_{EI}$ indicates connection from inhibitory to excitatory neuron), $\mathbf{h}_s$ is the input, with $s$ either 1 or 2 (corresponding to left and right licks), and $\xi$ is trial to trial noise, taken to be zero mean and Gaussian, with covariance matrices

$$\langle \xi_E \xi_E \rangle = \mathbf{\Sigma}_{EE}$$
$$\langle \xi_I \xi_I \rangle = \mathbf{\Sigma}_{II}.$$

For the input we'll assume that about half the elements of $h_s$ are $h_0$ for the rightward choice and $-h_0$ for the leftward choice, and the rest are $-h_0$ for the rightward choice and $h_0$ for the leftward choice. We used $h_0 = 0.1$. The noise covariance is diagonal but non-identity, with diagonal elements distributed as

$$\sqrt{\Sigma_{EE,ii}} \sim \text{Unif}\left(\sigma - \frac{\delta}{2}, \sigma + \frac{\delta}{2}\right)$$

$$\sqrt{\Sigma_{II,ii}} \sim \text{Unif}\left(\sigma - \frac{\delta}{2}, \sigma + \frac{\delta}{2}\right).$$

The goal is to determine the value of $s$ (that is, determine whether $\mathbf{h}_1$ or $\mathbf{h}_2$ was present) given the activity of a subset of the neurons from either the excitatory or inhibitory populations. We'll work in steady state, for which

$$\mathbf{v}_E = \mathbf{W}_{EE} \cdot \mathbf{v}_E - \mathbf{W}_{EI} \cdot \mathbf{v}_I + \mathbf{h}_s + \xi_E$$
$$\mathbf{v}_I = \mathbf{W}_{IE} \cdot \mathbf{v}_E - \mathbf{W}_{II} \cdot \mathbf{v}_I + \xi_I.$$

Solving for $\mathbf{v}_E$ and $\mathbf{v}_I$ yields

$$\mathbf{v}_E = \mathbf{J}_E \cdot \left(\mathbf{h}_s + \xi_E - \tilde{\mathbf{W}}_{EI} \cdot \xi_I\right)$$

$$\mathbf{v}_I = \mathbf{J}_I \cdot \left(\xi_I + \tilde{\mathbf{W}}_{IE}(\mathbf{h}_s + \xi_E)\right)$$

where

$$\mathbf{J}_E \equiv \left( \mathbf{I} - \mathbf{W}_{EE} + \tilde{\mathbf{W}}_{EI} \cdot \mathbf{W}_{IE} \right)^{-1}$$

$$\mathbf{J}_I \equiv \left( \mathbf{I} + \mathbf{W}_{II} + \tilde{\mathbf{W}}_{IE} \cdot \mathbf{W}_{EI} \right)^{-1}$$

$$\tilde{\mathbf{W}}_{EI} \equiv \mathbf{W}_{EI} (\mathbf{I} + \mathbf{W}_{II})^{-1}$$

$$\tilde{\mathbf{W}}_{IE} \equiv \mathbf{W}_{IE} (\mathbf{I} - \mathbf{W}_{EE})^{-1},$$

and $\mathbf{I}$ is the identity matrix. We are interested in the decoding accuracy of a sub-population of neurons. For that we'll use a matrix $\mathbf{D}_n$ that picks out $n$ components of whatever it's operating on. So, for instance, $\mathbf{D}_n \cdot \mathbf{\nu}_E$ is an $n$-dimensional vector with components equal to $n$ of the components of $\mathbf{\nu}_E$.

For a linear and Gaussian model such as ours, in which the covariance is independent of $s$, we need two quantities to compute the performance of an optimal decoder: the difference in the means of the subsampled populations when $\mathbf{h}_1$ versus $\mathbf{h}_2$ are present, and covariance matrix of the subsampled populations. The difference in means are given by

$$\Delta \langle \mathbf{D}_n \cdot \mathbf{\nu}_E \rangle = \mathbf{D}_n \cdot \mathbf{J}_E \cdot \Delta \mathbf{h}$$

$$\Delta \langle \mathbf{D}_n \cdot \mathbf{\nu}_I \rangle = \mathbf{D}_n \cdot \mathbf{J}_I \cdot \tilde{\mathbf{W}}_{IE} \cdot \Delta \mathbf{h}$$

where $\Delta \mathbf{h}$ is the difference between the two inputs,

$$\Delta \mathbf{h} \equiv \mathbf{h}_1 - \mathbf{h}_2.$$

The covariances are given by

$$\text{Cov}[\mathbf{D}_n \cdot \mathbf{\nu}_E] = \mathbf{D}_n \cdot \mathbf{J}_E \cdot \left[ \Sigma_{EE} + \tilde{\mathbf{W}}_{EI} \cdot \Sigma_{II} \cdot \tilde{\mathbf{W}}_{EI}^T \right] \cdot \mathbf{J}_E^T \cdot \mathbf{D}_n^T$$

$$\text{Cov}[\mathbf{D}_n \cdot \mathbf{\nu}_I] = \mathbf{D}_n \cdot \mathbf{J}_I \cdot \left[ \Sigma_{II} + \tilde{\mathbf{W}}_{IE} \cdot \Sigma_{EE} \cdot \tilde{\mathbf{W}}_{IE}^T \right] \cdot \mathbf{J}_I^T \cdot \mathbf{D}_n^T$$

where $T$ denotes transpose. Combining the mean and covariance gives us the signal to noise ratio,

$$(S/N)_E = \Delta \mathbf{h} \cdot \mathbf{J}_E^T \cdot \mathbf{D}_n^T \cdot \left( \mathbf{D}_n \cdot \mathbf{J}_E \cdot \left[ \Sigma_{EE} + \tilde{\mathbf{W}}_{EI} \cdot \Sigma_{II} \cdot \tilde{\mathbf{W}}_{EI}^T \right] \cdot \mathbf{J}_E^T \cdot \mathbf{D}_n^T \right)^{-1} \cdot \mathbf{D}_n \cdot \mathbf{J}_E \cdot \Delta \mathbf{h}$$

$$(S/N)_I = \Delta \mathbf{h} \cdot \tilde{\mathbf{W}}_{IE}^T \cdot \mathbf{J}_I^T \cdot \mathbf{D}_n^T \cdot \left( \mathbf{D}_n \cdot \mathbf{J}_I \cdot \left[ \Sigma_{II} + \tilde{\mathbf{W}}_{IE} \cdot \Sigma_{EE} \cdot \tilde{\mathbf{W}}_{IE}^T \right] \cdot \mathbf{J}_I^T \cdot \mathbf{D}_n^T \right)^{-1} \cdot \mathbf{D}_n \cdot \mathbf{J}_I \cdot \tilde{\mathbf{W}}_{IE} \cdot \Delta \mathbf{h} .$$

The performance of an optimal decoder is then given by

$$\text{fraction correct} = \Phi \left( \frac{\sqrt{S/N}}{\sqrt{2}} \right)$$

where $\Phi$ is the cumulative normal function. All of our analysis is based on this expression. Differences in fraction correct depend only on differences in the connectivity matrices, which we describe next.

### Connectivity matrices

We consider three connectivity structures: completely non-selective, signal-selective, and signal-to-noise selective (corresponding to Figures 5A–5C, respectively). In all cases the connectivity is sparse (the connection probability between any two neurons is 0.1). What differs is the connection strength when neurons are connected. We describe below how the connection strength is chosen for our three connectivity structures.

#### Non-selective

The connectivity matrices have the especially simple form

$$\mathbf{W}_{\alpha\beta,ij} = \begin{cases} \dfrac{w_{\alpha\beta}}{\sqrt{cN}} & \text{with probability } c \\\\ 0 & \text{otherwise} \end{cases}$$

where $\alpha, \beta \in \{E, I\}$, $N (\equiv N_E + N_I)$ is the total number of neurons, and $w_{\alpha\beta}$ are parameters.

#### Signal-selective

We divide the neurons into two sets of excitatory and inhibitory sub-populations, as in Figure 5B. The connection strengths are still given by the above expression, but now $\alpha$ and $\beta$ acquire subscripts that specify which population they are in: $\alpha, \beta \in \{E_1, E_2, I_1, I_2\}$, with $E_1$ and $I_1$ referring to population 1 and $E_2$ and $I_2$ to population 2. The within-population connection strengths are the same as for the non-selective population ($w_{\alpha_i\beta_i} = w_{\alpha\beta}$, $i = 1, 2$), but the across-population connection strengths are smaller by a factor of $\rho$,

$$\frac{w_{\alpha_i, \beta_j}}{w_{\alpha_i, \beta_i}} = \rho$$

for $i = 1$ and $j = 2$ or vice-versa. The value of $\rho$ determines how selective the sub-populations are: $\rho = 0$ corresponds to completely selective sub-populations while $\rho = 1$ corresponds to the completely non-selective case.

### SNR- selective

We choose the connectivity as in the non-selective case, and then change synaptic strength so that the inhibitory neurons receive stronger connections from the excitatory neurons with high signal to noise ratios. To do that, we first rank excitatory units in order of ascending signal to noise ratio (by using $\mathbf{D}_1$ in the expression for $(S/N)_E$ in the previous section).

$$W_{IE,ij} \rightarrow W_{IE,ij} \left( \frac{r_j}{N_E} \right)^4$$

where $r_j$ is the rank of excitatory $j$ in the order of ascending signal to noise ratio and, recall, $N_E$ is the number of excitatory neurons. This downweights projections from low signal to noise ratio excitatory neurons and upweights connections from high signal to noise ratio neurons. Finally, all elements are scaled to ensure that the average connection strength from the excitatory to the inhibitory network is the same as before the substitution.

### Simulation details

- Noise level $(\sigma)$ = 1.25
- Breadth of noise level distribution $(\delta)$ = 0.75
- Excitatory $\rightarrow$ excitatory coupling $(w_{EE})$ = 0.25
- Inhibitory $\rightarrow$ inhibitory coupling $(w_{II})$ = $-2$
- Excitatory $\rightarrow$ inhibitory coupling (reference) $(w_{IE}^{(0)})$ = 0.87
- Inhibitory $\rightarrow$ excitatory coupling (reference) $(w_{EI}^{(0)})$ = $-0.87$
- Connection probability $(c)$ = 0.1
- Number of excitatory neurons $(N_E)$ = 4000
- Number of inhibitory neurons $(N_I)$ = 1000
- Number of readout neurons $(n)$ = 50
- Input strength $(h_0)$ = 0.1
- Selectivity index $(\rho)$ = 0.75

The simulation parameters are indicated above. In addition, there are a number of relevant details, the most important of which is related to the input, $\mathbf{h}_s$. As mentioned in the previous section, about half the elements of $\mathbf{h}_s$ are $h_0$ for the rightward choice and $-h_0$ for the leftward choice, and the rest are $h_0$ for the leftward choice $-h_0$ for the rightward choice. This is strictly true for the completely non-selective and signal to noise selective connectivity; for the signal selective connectivity, we use $\mathbf{h}_{s,i} = h_0$ for the rightward choice and $-h_0$ for the leftward choice when excitatory neuron $i$ is in population 1, and $\mathbf{h}_{s,i} = h_0$ for the leftward choice and $-h_0$ for the rightward choice when excitatory neuron $i$ is in population 2. In either case, however, this introduces a stochastic element: for the completely non-selective and signal to noise selective connectivities, there is randomness in both the input and the circuit; for the signal selective connectivity, there is randomness in the circuit. In the former case, we can eliminate the randomness in the connectivity by averaging over the input, as follows.

Because the components of $\Delta\mathbf{h}$ are independent, we have

$$\langle \Delta h_{s,i} \Delta h_{s,j} \rangle = \delta_{ij} \langle \Delta h_{s,i}^2 \rangle$$

where $\delta_{ij}$ is the Kronecker delta ($\delta_{ij} = 1$ if $i = j$ and zero otherwise). Because $\Delta h_{s,i}$ is either $+h_0$ or $-h_0$, we have

$$\langle \Delta\mathbf{h}\Delta\mathbf{h} \rangle = 4h_0^2 \mathbf{I}$$

where $\mathbf{I}$ is the identity matrix. Thus, when we average the signal to noise ratios over $\Delta\mathbf{h}$, the expressions simplify slightly,

$$\frac{\langle (S/N)_E \rangle}{4h_0^2} = \text{trace} \left\{ \left( \mathbf{D}_n \cdot \mathbf{J}_E \cdot \left[ \mathbf{\Sigma}_{EE} + \tilde{\mathbf{W}}_{EI} \cdot \mathbf{\Sigma}_{II} \cdot \tilde{\mathbf{W}}_{EI}^T \right] \cdot \mathbf{J}_E^T \cdot \mathbf{D}_n^T \right)^{-1} \cdot \mathbf{D}_n \cdot \mathbf{J}_E \cdot \mathbf{J}_E^T \cdot \mathbf{D}_n^T \right\}$$

$$\frac{\langle (S/N)_I \rangle}{4h_0^2} = \text{trace} \left\{ \left( \mathbf{D}_n \cdot \mathbf{J}_I \cdot \left[ \mathbf{\Sigma}_{II} + \tilde{\mathbf{W}}_{IE} \cdot \mathbf{\Sigma}_{EE} \cdot \tilde{\mathbf{W}}_{IE}^T \right] \cdot \mathbf{J}_I^T \cdot \mathbf{D}_n^T \right)^{-1} \cdot \mathbf{D}_n \cdot \mathbf{J}_I \cdot \tilde{\mathbf{W}}_{IE} \cdot \tilde{\mathbf{W}}_{IE}^T \cdot \mathbf{J}_I^T \cdot \mathbf{D}_n^T \right\}.$$

To avoid having to numerically average over input, we used these expressions when computing decoding accuracy for the completely non-selective and signal to noise selective connectivity. That left us with some randomness associated with the networks (as connectivity is chosen randomly), but that turned out to produce only small fluctuations, so each data point in Figures 5A and 5C was from a single network. For the signal selective connectivity (Figure 5B), the network realization turned out to matter, so we averaged over 25 networks, and for each of them we did a further averaging over 100 random picks of the 50 neurons from which we decoded.

In Figure 5, the x axis is the ratio of the average connection strength from excitatory to inhibitory neurons to the average connection strength from inhibitory to excitatory neurons. This was chosen because it turned out to be the connectivity parameter with the largest effect on decoding accuracy. That in turn is because it turns out to be equivalent to the input noise to the inhibitory population. To see why, make the substitution

$$\mathbf{W}_{IE} \to \gamma \mathbf{W}_{IE}$$
$$\mathbf{W}_{EI} \to \gamma^{-1} \mathbf{W}_{EI}.$$

By letting $\nu_I \to \gamma \nu_I$, we see that this is formally equivalent to letting $\xi_I \to \gamma^{-1} \xi_I$, which in turn corresponds to letting $\Sigma_{II} \to \gamma^{-2} \Sigma_{II}$. Thus the x axis in Figure 5 can be thought of as the axis of decreasing input noise to the inhibitory neurons.

We produced a range of values for $\gamma$ by changing the coupling strengths between excitatory and inhibitory populations, while keeping their product constant at a reference value

$$w_{IE} w_{IE} = w_{IE}^{(0)} w_{EI}^{(0)}$$

### Immunofluorescence staining for TdTomato and GABA

To determine the fraction of inhibitory neurons that were labeled in our experiments, we performed double Immunofluorescence (IF) staining using antibodies against tdTomato (anti-RFP(tdTomato) Rockland 600-401-379) and GABA (anti-GAD67(GABA) MAB5406, EMD Millipore). Also, we used DAPI to stain the nuclei (Figure S15; GABA: green; tdTomato: red; DAPI: blue). 5 coronal sections which included the area PPC (Allen Brain Atlas) were used to quantify the fraction of overlap between GABA and tdTomato. We found GABA and tdTomato highly colocalized (Figures S15B–S15D; red and green are co-expressed in the vast majority of cells): 98.2% of tdTomato neurons expressed GABA, and all of the GABAergic neurons expressed tdTomato. These results indicate a very high level of selectivity and specificity for the labeling of inhibitory neurons in GAD-Cre;Ai14 mice, confirming original reports for these transgenic lines (Taniguchi et al., 2011).

### QUANTIFICATION AND STATISTICAL ANALYSIS

Our simultaneous imaging and decision-making dataset includes 135 sessions from 4 mice (45, 48, 7, and 35 sessions per mouse). Median number of trials per session is 213, 253, 264, and 222, for each mouse. On average, 480 neurons were imaged per session, out of which ~40 neurons were inhibitory and ~330 were excitatory. Approximately 100 neurons per session were not classified as either excitatory or inhibitory since they did not meet our strict cell-type classification criteria (see below). In 3 of the mice, the same group of neurons was imaged throughout learning (35-48 training days).

All analyses were performed on inferred spiking activity. Traces were down-sampled, so each bin was the non-overlapping moving average of 3 frames (97.1 ms, which we refer to as 97 ms). Inferred spiking activity for each neuron was normalized so the max spiking activity for each neuron equaled 1. The trace of each trial was aligned to the time of the choice (i.e., the time of the 1st lick to either of the side waterspouts after the go tone). Two-tailed t test was performed for testing statistical significance. Summary figures including all mice were performed on the time bin preceding the choice, i.e., 0-97 ms before choice onset. All reported correlations are Pearson's coefficients. Analyses were performed in Python and MATLAB.

### DATA AND CODE AVAILABILITY

All the data used in the paper are publicly available on CSHL repository: http://repository.cshl.edu/36980/. Further, all the data is converted into the NWB format (Neurodata Without Boarders; Teeters et al., 2015; Rübel et al., 2019), and is available on CSHL repository: http://repository.cshl.edu/id/eprint/37693

Code for data processing and analysis is publicly available on github: https://github.com/farznaj/imaging_decisionMaking_exc_inh

Code for converting data to NWB format is also available on github: https://github.com/vathes/najafi-2018-nwb